

The role of clear sky identification in the study of cloud radiative effects: 26  
combined analysis from ISCCP and the Scanner of Radiation Budget (ScaRaB)

C. J. STUBENRAUCH and V. BRIAND

Laboratoire de Météorologie Dynamique, Ecole Polytechnique

F-91128 Palaiseau cedex, France

W. B. ROSSOW

NASA Goddard Institute for Space Studies

2880 Broadway, New York, NY-10025, U.S.A.

submitted to Journal of Applied Meteorology

January 2001



## ABSTRACT

Since the effect of clouds on the earth's radiation balance is often estimated as the difference of net radiative fluxes at the top of the atmosphere between all situations and monthly averaged clear sky situations of the same regions, a reliable identification of clear sky is important for the study of cloud radiative effects. The Scanner for Radiation Balance (ScaRaB) radiometer on board the Russian Meteor-3/7 satellite provided earth radiation budget observations from March 1994 to February 1995 with two ERBE-like broad-band longwave and shortwave channels. Two narrow-band channels, in the infrared atmospheric window and in the visible band, have been added to the ScaRaB instrument to improve the cloud scene identification. The International Satellite Cloud Climatology Project (ISCCP) method for cloud detection and determination of cloud and surface properties uses the same narrow-band channels as ScaRaB, but is employed to a collection of measurements at a better spatial resolution of about 5 km. By applying the original ISCCP algorithms to the ScaRaB data, the clear sky frequency is about 5% lower than the one over quasi-simultaneous original ISCCP data, an indication that the ISCCP cloud detection is quite stable. However, one would expect an about 10 to 20% smaller clear sky occurrence over the larger ScaRaB pixels. Adapting the ISCCP algorithms to the reduced spatial resolution of 60 km and to the different time sampling of the ScaRaB data leads therefore to a reduction of a residual cloud contamination. A sensitivity study with time-space collocated ScaRaB and original ISCCP data at a spatial resolution of  $1^\circ$  longitude x  $1^\circ$  latitude shows that the effect of clear sky identification method plays a higher role on the clear sky frequency and therefore on the statistics than on the zonal mean values of the clear sky fluxes. Nevertheless, the zonal outgoing longwave fluxes corresponding to ERBE clear sky are in general about 2 to 10  $\text{Wm}^{-2}$  higher than those obtained from the ScaRaB adapted ISCCP clear sky identifications.

The latter are close to (about  $1 \text{ Wm}^{-2}$  higher) fluxes corresponding to clear sky regions from original ISCCP data, whereas ScaRaB clear sky LW fluxes obtained with the original ISCCP identification lie about 1 to  $2 \text{ Wm}^{-2}$  below. Especially in the tropics where water vapor abundance is high, the ERBE clear sky LW fluxes seem to be systematically overestimated by about  $4 \text{ Wm}^{-2}$ , and SW fluxes are lower by about 5 to  $10 \text{ Wm}^{-2}$ . However, the uncertainty in the analysis of monthly mean zonal cloud radiative effects is also produced by the low frequency of clear sky occurrence, illustrated when averaging over pixels or even over regions of  $4^\circ$  longitude x  $5^\circ$  latitude, corresponding to the spatial resolution of General Circulation Models. The systematic bias in the clear sky fluxes is not reflected in the zonal cloud radiative effects, because the clear sky regions selected by the different algorithms can occur in different geographic regions with different cloud properties.

## 1. Introduction

Clouds have an important impact on the energy distribution in the atmosphere mainly through two mechanisms: on one hand they cool the earth (mostly the surface) by reflecting solar radiation, and on the other hand they warm the earth (mostly the atmosphere) by partially capturing emitted thermal radiation. A first estimation of the importance of these effects was determined by comparing incoming and outgoing fluxes at the top of the atmosphere (TOA) between all situations and monthly averaged clear sky situations in the same regions (Charlock et al. 1985). The Earth Radiation Budget Experiment (ERBE, Barkstrom et al. 1989) has shown that, in the global annual mean, clouds cool the earth by about  $20 \text{ Wm}^{-2}$  (Harrison et al. 1990). However, regionally and seasonally radiative effects of clouds can be quite different, depending on their physical properties (cf. Stephens et al. 1991, Ockert-Bell et al. 1992, Stubenrauch et al. 1999, Chen et al. 2000). As the geographical and temporal distributions of the radiative fluxes at TOA are directly linked to the global circulation of the atmosphere and oceans, the difference between clear sky and cloudy fluxes has been widely used to test the realism of climate models (cf. Cess and Potter 1987, Harshvardhan et al. 1989, Ridout et al. 1994). Therefore, a reliable identification of clear sky situations is important. Several studies (Hartmann and Doelling 1991, Rossow and Zhang 1995, Collins et al. 1995, Stubenrauch et al. 1997, Chen et al. 2000) suggest that ERBE clear sky longwave (LW) fluxes tend to be biased high, especially in tropical regions where atmospheric water vapor is abundant.

The ScaRaB radiometer on board the Russian Meteor-3/7 satellite provided measurements of reflected solar radiation and emitted thermal radiation at TOA from March 1994 to February 1995 (Viollier et al. 1995, Kandel et al. 1998) with two ERBE-like broad-band LW and shortwave (SW) channels. The inclination of the orbit ( $82.6^\circ$ ) is such that all local hours

are observed within 104 days. Measured broad-band radiances are currently converted into radiative fluxes by the ERBE inversion algorithm (Smith et al. 1986). Scene dependent angular corrections play an important part in the inversion. A reliable scene identification is not only important for angular dependence models (ADM's), but also for studying cloud radiative effects, as explained above. Two additional ScaRaB narrow-band channels, centered on the 11.5  $\mu\text{m}$  infrared (IR) atmospheric window and on the 0.6  $\mu\text{m}$  visible (VIS) band, should allow an improvement of the cloud scene identification because the contrast between clouds and the surface is better for these narrow-band channels than for the broad-band channels.

A regional study (Stubenrauch et al. 1996) has already shown that the ScaRaB narrow-band channels make it possible, even at the relatively low ScaRaB spatial resolution of about 60 km (at nadir), to establish a more detailed cloud field identification than ERBE. On the other hand, in order to obtain a cloud scene identification which is reliable over the whole globe it is better to start from already developed cloud detection algorithms which are functioning globally.

The ISCCP (International Satellite Cloud Climatology Project) method for cloud detection and determination of cloud and surface properties makes use of the same narrow-band channels as ScaRaB, but is applied to a collection of measurements at a better spatial resolution of about 5 km, from geostationary and polar orbiting satellites around the globe (Rossow and Schiffer 1991, Rossow and Schiffer 1999). Even if the initial spatial resolution of these measurements is much better, the ISCCP cloud detection method is a good starting point for an improved ScaRaB scene identification. Therefore, this method was applied to the ScaRaB VIS and IR radiances for cloud detection and for the determination of their properties.

The different clear sky identification methods are described in Section 2. First, the original ERBE and ISCCP clear sky identifications are considered. Then, the ISCCP algorithm is adjusted to account for the ScaRaB reduced spatial resolution, Finally we present a newly developed algorithm which also takes into account the different time sampling of the ScaRaB data. Section 3 compares results on clear sky frequencies and clear sky LW fluxes at TOA obtained with these four clear sky identification methods. A sensitivity study with time-space collocated ScaRaB and ISCCP data evaluates the effect of clear sky identification method and of statistical averaging on clear sky frequency and on clear sky fluxes at TOA. Section 4 discusses the effect of statistics on the analysis of cloud radiative effects. Conclusions are given in Section 5.

## **2. Clear sky identification methods**

### ***a. ERBE scene identification***

The ERBE scene identification (Wielicki and Green 1989) is based on a maximum likelihood method applied on the broad-band LW and SW radiances. Scenes are grouped into four different classes depending on cloud cover: from clear sky, described by the warmest and darkest scenes, over partly cloudy and mostly cloudy to overcast, which is described by the coldest and brightest scenes. Kernels that vary with latitude and season for these scenes have been pre-determined for five different geotypes (ocean, land, desert, coast and snow); see Hartmann and Doelling (1991) discussion about the effects of kernels that are constant for whole seasons. This cloud scene identification is used to choose angular dependence models for the conversion of radiances into fluxes. The ERBE clear sky identification has also been extensively used for the study of the radiative effects of clouds (see Section 1).

### ***b. ISCCP cloud detection***

ISCCP cloud detection and classification is based on a series of variable threshold tests applied to narrow-band IR and VIS radiances. These narrow-band radiances exhibit a better contrast between clouds and surface and are therefore better suited for cloud detection than broad-band radiances (cf. Rossow et al. 1989).

Clouds are detected through a final IR-VIS threshold test comparing the measured radiances to clear sky composite radiances which have been determined from pixels that exhibit low IR spatial and temporal variability (Rossow and Garder 1993a). The main part of the algorithm consists in the determination of clear sky composite radiances for each pixel. These reference clear sky radiances come from the locally warmest pixels (within 8 K over land and 3.5 K over ocean) over an area of about 100 km x 100 km over land (3 x 3 pixels) and about 450 km x 450 km (15 x 15 pixels) over tropical ocean to 270 km (latitude) x 750 km (longitude) (9 x 25 pixels) over midlatitude ocean that also have similar temperatures (within 2.0 K over land and 1.0 K over ocean) compared to values at the same location on the previous and the following day at the same time. The spatial variability threshold  $\Delta 1$  decides between a cloudy and an undetermined pixel, whereas the temporal variability thresholds  $\Delta 2$  and  $\Delta 3$  decide if the pixel is clear or cloudy/undetermined. Short- and long-term clear sky statistics are collected respectively over 5/15 days over land and over 15/30 days over ocean. These results are then analyzed by taking into account the geotype variability characteristics to determine the clear sky composite radiances. The final scene identification is a comparison of each measured radiance to its clear sky composite value. The different thresholds are summarized in Table 1.

For cloudy pixels, cloud top temperature and optical thickness (only during day) are determined, using a radiative transfer model which assumes cold ( $T < 260$  K) ice clouds are

made of 30  $\mu\text{m}$  polycrystals and warm liquid clouds are made of 10  $\mu\text{m}$  spheres (Rossow and Schiffer 1999). Cloud top temperature is transformed into cloud top pressure using TOVS operational temperature profiles.

Whereas the size of the pixels used by the ERBE algorithm is about 60 km, the ISCCP algorithm has been developed to use pixels with a size of about 5 to 8 km. One ScaRaB pixel can be represented by about four ISCCP pixels, assuming that the sampling of the latter is such that they represent the characteristics of the whole region of 60 km x 60 km (Sèze and Rossow 1991). Differences in pixel size and in sampling between ScaRaB and ISCCP data are illustrated in Fig. 1. These differences will particularly influence the spatio-temporal statistics used for the determination of clear sky composites in the ISCCP algorithm, which will be studied in more detail in Section 2.3.

The original ISCCP algorithms have been applied to the whole ScaRaB data set. The pixel data have been put onto a grid with a spatial resolution of  $1/3^\circ$ , corresponding to  $4/3$  of the initial spatial resolution of ISCCP data. ISCCP cloud detection and determination of cloud properties are then carried out the same way as for data from a polar orbiting satellite.

### *c. ISCCP cloud detection adapted to ScaRaB spatial resolution*

An increase of pixel size from 5 to 60 km leads to an increase of surface and cloud variability that is counteracted by effects of averaging over the larger pixel area. However, both effects serve to reduce the radiance contrast between cloudy and clear scenes, producing more cloud contamination of clear pixels. This tendency is reinforced by an increasing probability for mixtures of cloud and clear scenes to occur within the larger pixel, especially for low-level clouds (cf. Wielicki and Parker 1992). To illustrate these effects, we first

compare in Fig. 2 the IR brightness temperature distributions from original ISCCP data and from ScaRaB pixels of all scenes and of scenes identified as clear sky. The ISCCP data have been processed using measurements from the AVHRR (Advanced Very High Resolution Radiometer) instrument on board the polar orbiter NOAA-12. For the second half of March 1994, the observation time of both satellites is quite similar. From 24 to 26 March the crossing time at the equator of 7h30 am is within a few minutes for the two satellites. The observation time coincidence is the best at low latitudes ( $< 30^\circ$ ), because the two satellites METEOR-3/07 and NOAA-12 are orbiting the earth in opposite directions.

The standard deviation for all AVHRR pixels (Fig. 2a) is slightly higher than for ScaRaB pixels (Fig. 2c), by about 1.3 K, indicating that the averaging effect dominates the increased variability over this particular range of spatial scales. The mean values are, as expected nearly the same. However, when considering only the clear sky scenes, the standard deviation of ScaRaB clear sky scenes (Fig. 2d) is slightly higher (by about 1.3K) and the mean value slightly lower (by about 1.2 K), indicating a small cloud contamination of the ScaRaB pixels which have been identified as clear sky.

Since the absolute values also depend on the clear sky statistics of different geographical regions, we will compare for the adaptation of the ISCCP cloud detection algorithm the *relative* brightness temperatures and reflectances, obtained by subtraction of the clear sky composite values. The distribution of clear sky brightness temperatures around the clear sky composite in Fig. 3 should represent the spatial and temporal variability of the surface. If one compares in Figs. 3a and 3b the distributions of the original ISCCP data and of simulated ScaRaB pixels (by an accumulation of four adjacent ISCCP pixels, see Fig. 1), one can clearly see the expected decrease in surface variability of about 0.7 K due to averaging over the larger pixel size. Yet, one observes in Fig. 3c a larger standard deviation (by 0.2 K) of the

distribution of ISCCP-detected clear sky over ScaRaB pixels than for the original ISCCP data, reflecting increased cloud contamination.

The thresholds in the ISCCP cloud detection have to be adjusted so that the relative clear sky brightness temperature distribution looks similar to the one for the simulated ScaRaB pixels in Fig. 3b. The algorithm adjustment must take into account that the spatial and temporal variability of the surface characteristics is smaller for the larger ScaRaB pixels. Therefore, thresholds used in the space/time variability test (the first part of the ISCCP algorithm) must be reduced. Since the test on spatial variability results only in a distinction between a cloudy and undetermined scene (Rossow and Garder 1993a) and since the behavior of spatial variability cannot be easily estimated, because the regions covering the same number of pixels are larger and therefore offset the decrease in variability, only thresholds used in the temporal variability test are altered. These have been reduced by about 1/2 of their original values (Table 1).

The second part of the algorithm to be modified is the clear sky composite radiance determination. The relation between the extremes and the average clear sky radiances, specific to each geotype, depends again on the spatial resolution, either for short- or long-term statistics (Seze and Rossow 1991; Rossow and Garder 1993a). Table 1 summarizes the new thresholds which have been reduced by approximately 1/3.

With these modifications a new distribution of clear sky brightness temperatures around the clear sky composite values is obtained, shown in Fig. 3d. The right side of the distribution, corresponding to the warmest pixels, now similar to the simulated ScaRaB pixels in Fig. 3b. This indicates that the clear sky composite radiances are now adequate as a reference for scene identification. After adjusting the final clear sky thresholds (Table 1) the entire distribution now looks like the one for the four merged ISCCP pixels.

In the case of the visible radiances, the adjustment is more difficult because the viewing geometry is not exactly the same due to the opposite orbits. Therefore, the adjustment of VIS thresholds is made by the same amount as the IR radiances, shown in Table 1.

*d. Cloud detection adapted to ScaRaB temporal resolution*

Another difference between the original ISCCP data and ScaRaB data is the temporal resolution. The ISCCP cloud detection was initially developed for measurements on satellites which observe a given location at the same time of the day, allowing for most precise statistics for the clear sky composites (Rossow and Garder 1993b). Since for the Meteor satellite the observation time shifts by about three hours over a month, the longer-term statistics of clear sky composites should be more difficult to establish, especially for geographical regions where the diurnal cycle has a large amplitude like deserts. The ScaRaB observation time is explicitly presented for every month in Capderou (1995). During the month of March 1994, the observation time shifts from about 10h30 to 6h30 at the equator.

In order to take this time shift properly into account, a new algorithm has been developed in which clear sky composite radiances are now determined from statistics from all regions of the same geotype instead of using time statistics (during 15/30 days) for the same location.

## **1) DETERMINATION OF CLEAR SKY COMPOSITES**

The first step consists of defining a more detailed geotype classification than used by the ISCCP algorithm, since for the determination of the clear sky composite radiances it is necessary to compare the brightness temperatures and reflectances over regions for which one would expect a similar clear sky behavior. On the other hand, the population of samples

over the region must be large enough in order to assure the presence of a pixel with clear sky. Starting from the CERES/SARB (Cloud and the Earth's Radiant Energy System/ Surface and Atmospheric Radiation Budget) geotype classification (Rutan et al. 1997), which includes 18 geotypes at a spatial resolution of  $1/6^\circ$ , we merge these into nine geotypes over land, presented in Table 2. Note that for the identification of snow and ice covered scenes, the ISCCP information is directly used in order to take into account seasonal variations. The geotype 'ocean' is split into twelve  $30^\circ$  longitude bands, leading to oceanic regions with similar airmasses. The final classification, consisting of 21 land and ocean types, represents a compromise between the sample size requirement and climatic homogeneity.

For each type, the clear sky composites are determined as a function of latitude for IR and as a function of viewing geometry for VIS radiances. The reference values (maximum IR and minimum VIS radiances) will be determined over a short time period in order to eliminate effects due to the shift of the observation time.

First we study the importance of sample population for establishing stable references of clear sky brightness temperature composites. If the sample size is not large enough, there is a risk that there is no clear sky scene over the observed geotype. In this case, the maximum brightness temperature,  $T_B^{\text{ref}}$ , will correspond to a cloudy scene and be biased low. On the other hand, if the chosen geotype covers a region which is too large,  $T_B^{\text{ref}}$  corresponds just to the warmest sub-region (for example caused by a marine current). In this case, the colder clear sky scenes in the rest of the region would be considered as cloudy. In the following, the effects of the width of the latitude band and of the length of the time period on the determination of the clear sky IR composites are studied.

Fig. 4 shows the reference clear sky brightness temperatures,  $T_B^{\text{ref}}$ , as a function of latitude obtained from statistics over a latitude band corresponding to two ScaRaB pixels ( $2/3^\circ$ ) and

to three ScaRaB pixels ( $1^\circ$ ) and over a time period of one day and of three days for evergreen forest, grassland and for two ocean regions. The maximum brightness temperature is only kept as  $T_B^{\text{ref}}$  if it came from a sample of more than nine values in order to reduce the probability of cloud contamination. Then  $T_B^{\text{ref}}$  is smoothed as a function of latitude for each geotype in order to eliminate values too far from the mean and to fill in the missing values. From Fig. 4 one deduces that one should use a statistics over three days, because in regions with frequent cloudiness, especially in the tropics,  $T_B^{\text{ref}}$  could be easily underestimated by up to 5 K by using statistics of only one day. The effect of the width of the latitude band is less important: a larger latitude band only smoothes the latitudinal behavior of  $T_B^{\text{ref}}$ . The necessity of a more detailed ocean classification into regions of restricted longitude is exposed in Fig. 5, showing zonal mean  $T_B^{\text{ref}}$  for all twelve ocean regions: At some latitudes  $T_B^{\text{ref}}$  can vary by up to 10K from one ocean region to the other.

The variation of  $T_B^{\text{ref}}$  due to the observation time shift of the Meteor satellite orbit is illustrated in Fig. 6 which shows  $T_B^{\text{ref}}$  as function of latitude for the same geotypes as in Fig. 4 at different time periods during March 1994. Statistics are collocated at each time over three days. One can see a decrease of  $T_B^{\text{ref}}$  of about 5 K to 10 K from the beginning of the month (observation at 10h30 am) to the end of the month (observation at 6h30 am).

In order to determine the VIS clear sky composite radiances for each geotype, the minimum within intervals of solar zenith angle, viewing zenith angles and relative azimuth angles is kept as the reference if it is obtained from a sample of more than nine values, and then the values are smoothed as in the case of the brightness temperatures but according to the different viewing / illumination angles instead of latitude.

## 2) FINAL CLEAR SKY DETECTION

Clear sky is identified by comparing 1) the measured brightness temperature  $T_B$  to the local maximum brightness temperature  $T_B^{9\text{pix}}$  over nine adjacent ScaRaB pixels and to  $T_B^{\text{ref}}$  (as function of latitude and geotype) and 2) the measured reflectance  $R_{\text{VIS}}$  to the local minimum reflectance  $R_{\text{VIS}}^{9\text{pix}}$  over nine adjacent ScaRaB pixels and to the reference reflectance  $R_{\text{VIS}}^{\text{ref}}$  (as function of observation geometry and geotype). Step 2 can be applied only to daytime measurements. As an example, Fig. 7 shows scatter plots of these variables, a)  $(T_B^{9\text{pix}} - T_B)/T_B^{9\text{pix}}$  and  $(T_B^{\text{ref}} - T_B)/T_B^{\text{ref}}$ , and b)  $(R_{\text{VIS}}^{9\text{pix}} - R_{\text{VIS}})/R_{\text{VIS}}^{9\text{pix}}$  and  $(R_{\text{VIS}}^{\text{ref}} - R_{\text{VIS}})/R_{\text{VIS}}^{\text{ref}}$  for the geotype evergreen forest. Pixels identified as clear sky by the adapted ISCCP algorithm described in Section 2c have been marked as light gray. These clear sky scenes are well bundled at low values of these four variables, whereas the cloudy pixels populate the space with higher values.

The *relative* thresholds are then determined for each geotype by comparing the distributions of these four variables to the distributions of the clear sky scenes obtained from the adapted ISCCP algorithm. By setting the thresholds to the mean plus one standard deviation of the ISCCP clear sky distributions, the agreement between both clear sky identifications is about 85% (90% over ocean). Agreement varies from 70% for bushland to 94% for evergreen forest. In this way, we use the ISCCP clear sky identification as a first reference, but since the methods are independent, the scene identifications are not directly correlated. Therefore initial errors in the ISCCP scene identification should influence the new method only randomly and not systematically.

### **3. Clear sky frequencies and clear sky TOA LW fluxes**

#### ***a. Clear sky frequencies and LW fluxes at pixel resolution***

To get a first impression of the ISCCP clear sky identification over ScaRaB pixels, we compare in Fig. 8 the resulting zonal clear sky frequencies (ScaRaB-ISCCP) to those obtained by the ERBE inversion (ScaRaB-ERBE) and to the original ISCCP clear sky frequencies (AVHRR-ISCCP). For this study we use quasi-simultaneous data covering the period from 24 to 26 March 1994 (see Section 2c).

From Fig. 8 one notices first that the ERBE clear sky frequency is systematically the smallest: especially in the tropics the difference reaches 20%. The difficulty of finding clear sky in the tropical regions with the ERBE algorithm can be explained by the fact that the broad-band channels are also sensitive to water vapor which is interpreted as thin cloud. On the other hand, the clear sky frequency found with the ISCCP algorithms over the ScaRaB pixels is quite close to the one observed over the AVHRR pixels, varying from 35% in the tropics to 55% in the desert regions. The average clear sky frequencies for ScaRaB-ISCCP are only about 5% smaller than for AVHRR-ISCCP, even though the pixel size is about 10 times larger. This result is puzzling, suggesting that the decision to declare a pixel cloudy or clear can be ambiguous or imprecise. Only when the pixel size is smaller than the smallest cloud does the cloud amount attain a constant value that represents the surface area really covered by clouds. The study of Wielicki and Parker (1992) on the evolution of the cloud amount with spatial resolution showed that the difference between ISCCP retrieved and real cloud amount increases from -10% to +2% with pixel size increasing from 1/32 to 8 km, the latter close to the AVHRR pixel size (1 km times 4 km in Global Area Coverage format) to which the algorithm is adapted. According to our study, for a 10 times lower spatial resolution, the

difference is only about 5%. This indicates the stability of the ISCCP cloud detection with spatial resolution, because the general cloud amount, which is the subtraction of the clear sky frequency from 100%, is about the same, regardless of which measurement is used. However, as illustrated before, this stability implies more cloud contamination of the clear radiances.

The clear sky frequency expected over a region of the size of ScaRaB pixels can be estimated by simulating the ScaRaB pixels by an accumulation of four adjacent ISCCP pixels. A composite of adjacent pixels will be declared clear only if all pixels are clear. Since the ISCCP pixels are sampled, the simulated ScaRaB clear sky frequency could be slightly overestimated in the case that small clouds hide just in the regions between the sampled AVHRR pixels, as illustrated in Fig. 1. The evolution of clear sky frequency with increasing pixel size (increasing number of merged ISCCP pixels) is presented in Fig. 9. From this figure one deduces that the clear sky frequency over ScaRaB pixels should be on average about 15% smaller than the clear sky frequency over ISCCP pixels. One notices that this evolution varies strongly with the observed region: in regions with clouds of large extent like in the deep convection zone over Indonesia ('Warm Pool') the difference is only 10%, whereas in regions with small stratocumulus clouds (ST) one finds a decrease of clear sky frequency of about 20%. The comparison with the only 5% smaller clear sky frequency observed in Fig. 8 confirms that for a clear sky identification without cloud contamination over ScaRaB pixels, as for the study of cloud radiative effects or for the development of ADM's, the test parameter values used at several places in the ISCCP algorithm have to be adjusted to the spatial resolution of the ScaRaB pixels as in Section 2c.

Clear sky frequencies, obtained from all four methods described in Section 2, are compared for the whole month of March 1994 in Fig. 10, separately for ocean and land and during day. In order to facilitate the comparison, differences are also shown between the first three

methods and the fourth method. By adapting the ISCCP method to the spatial resolution of the ScaRaB pixels, the clear sky frequency has been reduced in general by about 5 to 20%, in agreement with the simulation shown in Fig. 9. The clear sky identification method developed for the temporal sampling of ScaRaB gives results similar to the ISCCP method adapted to the spatial resolution of the ScaRaB pixels. This indicates that the consideration of seasonal shifts of clear sky temperatures in the ISCCP algorithm also works well for the temporal shift at ScaRaB scale. Nevertheless, the clear sky frequency has been slightly increased in regions with a strong diurnal cycle (subtropical land). The ERBE identification still yields the smallest clear sky frequency over ocean, especially in the tropics, where the water vapor abundance is high. Over land the situation is different, because ERBE detects about 20% more clear sky in the subtropics where most of the deserts are. The other clear sky identifications, which are based more on spatial and temporal variability than on the warmest and darkest scenes, detect less clear sky in these regions. The results for night measurements (not shown) are similar, with an even lower ERBE clear sky frequency over ocean, which leads to a difference in the tropics of 20%.

On the other hand, the clear sky LW fluxes (Figs. 11 for day and Fig. 12 for night measurements), obtained from all four methods described in Section 2, are more similar, the ISCCP clear sky identification yielding the lowest LW fluxes and ERBE the highest LW fluxes. The difference lies in general around  $5 \text{ Wm}^{-2}$ . In the tropics and during night, however, the difference can exceed  $10 \text{ Wm}^{-2}$ , indicating that the use of the narrow-band channels most probably leads to a more reliable scene identification. Note that in general the oceanic clear sky fluxes do not change from day to night (with exception of ERBE yielding higher nighttime clear sky fluxes), whereas clear sky fluxes in the dry subtropical zones are  $10$  to  $15 \text{ Wm}^{-2}$  smaller during night than during daytime. Over subtropical land in the

southern hemisphere, the ERBE algorithm identifies deserts as nearly always cloud free and yet produces a  $5 \text{ Wm}^{-2}$  lower clear sky LW flux. From Fig. 11 and Fig. 12 we also deduce that the adjustment of the ISCCP cloud detection to ScaRaB spatial resolution has a smaller effect on the clear sky LW fluxes than on the clear sky frequency. Even if the clear sky frequency has been reduced by 10 to 20%, taking out most scenes with residual cloud contamination, the clear sky fluxes increase by only  $2 \text{ Wm}^{-2}$  over ocean and up to  $10 \text{ Wm}^{-2}$  over tropical land. Note that over ocean the method which takes care of the ScaRaB temporal sampling gives nearly identical results to the adapted ISCCP method, whereas differences over land lie around  $3 \text{ Wm}^{-2}$ . Standard deviations of the zonally averaged clear sky fluxes are around  $10$  to  $15 \text{ Wm}^{-2}$  over land and less than  $10 \text{ Wm}^{-2}$  over ocean, slightly smaller for the newly developed method.

#### ***b. Clear sky frequencies and LW fluxes at GCM spatial resolution***

For a further evaluation of the cloud detection methods described in Section 2, the ScaRaB data have been combined with simultaneous (within 15 minutes) observations from the ISCCP data. The ISCCP data (DX series) are organized on a grid of  $1/4^\circ$ , compared to  $1/3^\circ$  for the ScaRaB data. Therefore, for the collocation, each dataset has been degraded to  $1^\circ$ . Since the coordinates of the ScaRaB pixels are given, like for ERBE pixels, at TOA, they had to be transformed to the surface coordinates used by ISCCP. The coordinate transformation, which depends on the viewing zenith angle, effects the instantaneous LW fluxes by up to  $2 \text{ Wm}^{-2}$  and the SW fluxes by up to  $10 \text{ Wm}^{-2}$  (Stubenrauch et al. 1999). Fluxes have been averaged over the  $1^\circ \times 1^\circ$  grid, whereas cloud and surface properties have been respectively averaged over cloudy and clear sky pixels. A  $1^\circ \times 1^\circ$  grid is declared as clear sky

when all pixels are clear. Another difficulty in the collocation process is that the exact observation time is not kept in the ISCCP climatology. For this reason we could collocate only daytime measurements, because the sun zenith angle could be used as a measure of observation time. This collocated dataset was created for the development of SW ADM's (Briand 2000).

The probability of clear sky extending over a region of  $1^\circ \times 1^\circ$  is only about two thirds as high as over  $60 \text{ km} \times 60 \text{ km}$  regions (Fig. 9) and thus the problem of low sample populations is even more aggravated. On the other hand, clear sky over larger regions consisting of several pixels detected as clear sky is probably more reliable than regions of one pixel. A sensitivity analysis can be done by first averaging the  $1^\circ$  clear sky fluxes over regions of  $4^\circ \times 5^\circ$  (the spatial resolution of many climate GCM's) and then calculating the zonal means. In this way, the weight between regions of low cloudiness and regions of high cloudiness will be more equal. This should give more stable results, especially in regions with low clear sky frequencies. In addition, these results can be more directly compared to results from GCM's, since these quantities can be computed in the same manner. The clear sky frequency then corresponds to the fraction of  $4^\circ \times 5^\circ$  regions which have clear sky extending over at least a  $1^\circ \times 1^\circ$  region.

Fig. 13 then presents the frequency of  $4^\circ \times 5^\circ$  regions with clear sky extending over at least  $1^\circ \times 1^\circ$ , determined from ScaRaB data using the four cloud detection methods described in Section 2, in comparison with results from the time-space collocated ISCCP data, separately for ocean and land during daytime. Again, differences are also shown for an easier comparison. The ScaRaB LW fluxes are appointed to collocated  $1^\circ \times 1^\circ$  clear sky scenes detected in the original ISCCP data.

Considering ocean, the largest clear sky frequency is found by the original ISCCP cloud

detection applied to ScaRaB data, indicating a residual cloud contamination. The clear sky frequency from the original ISCCP data is about 5 to 10% lower, but note that due to the sampling some clouds could be hidden, so this clear sky frequency estimate should be an upper limit for the comparison to clear sky for ScaRaB pixels. The frequencies from the threshold-adapted ISCCP cloud detection and from the ERBE algorithm are close and 5 to 10% lower than the result from original ISCCP data, with a larger difference in the tropics where clear sky regions are most probably smaller. Note that this time the lowest clear sky frequencies come from the newly developed ScaRaB cloud detection. The comparison of Fig. 13 and Fig. 10 indicates that the newly developed ScaRaB method yields smaller clear sky regions over ocean than the ERBE method.

For land the situation is more complicated. The tendencies are the same, with the exception of the desert zones where ERBE finds the most clear sky and the difference between original ISCCP and the ScaRaB-adapted cloud detections are larger due to broken cloudiness. Note that the clear sky frequency of the newly developed ScaRaB cloud detection is much closer again to the one of the ISCCP threshold-adapted method than over ocean.

Fig. 14 shows the zonal mean LW fluxes from  $1^\circ \times 1^\circ$  clear sky regions and averaged over  $4^\circ \times 5^\circ$  regions, together with differences. Over ocean, zonal LW fluxes corresponding to ERBE clear sky are in general about  $5 \text{ Wm}^{-2}$  higher than those obtained from the original ISCCP identification, the latter close to fluxes corresponding to clear sky regions from original ISCCP data. The algorithms adjusted to ScaRaB spatial and temporal resolution identify clear sky which is less contaminated with clouds and therefore produce slightly larger LW fluxes (by about 2 to  $3 \text{ Wm}^{-2}$ ). The situation over land looks similar as in Fig. 11. Note that at northern hemisphere midlatitudes latitudes the zonal mean ERBE clear sky flux is 5 to  $10 \text{ Wm}^{-2}$  higher than the one from the ScaRaB-adapted cloud detections. In these

regions, the sun is just rising, the mean solar zenith angle is larger than  $63^\circ$ . In these regions, the ERBE clear sky frequencies are also small. The difference between Fig. 14 and 11 could be explained by these effects.

#### **4. Cloud radiative effects**

##### ***a. Cloud radiative warming***

As mentioned in Section 1, a first estimate of the radiative warming effect of clouds can be obtained by analyzing the difference between the monthly averaged clear sky LW flux and the total LW flux for each region at TOA. This global cloud radiative warming effect takes into account the occurrence of clouds as well as variations of their physical properties like physical size, thickness and height. Since with observations one can only sample clear sky when clouds do not occur (Cess and Potter 1987, Harshvardan 1989), changes in the atmospheric state that are correlated with cloud occurrence are included in the determination of "cloud" radiative effects from satellite observations. In this section we are interested in results which can be directly compared to GCM's. Therefore we use, as in Section 3b, statistics over regions of  $4^\circ \times 5^\circ$ . Only regions are used for this analysis which have at least one  $1^\circ \times 1^\circ$  grid completely filled with clear sky pixels. Fig. 15 presents the cloud radiative warming as obtained from ScaRaB data for March 1994 during daytime (morning satellite pass), separately over land and ocean. As in Section 3, results from the different clear sky identifications are compared. During March 1994 the ScaRaB observation time shifts from 10h30 to 6h30. The cloud radiative warming is the highest over tropical land where it reaches  $30 \text{ Wm}^{-2}$  and  $23 \text{ Wm}^{-2}$  over tropical ocean. The intertropical convergence zone, with its frequent occurrence of high opaque clouds, is responsible for this effect. In the subtropics where clouds occur less often

and are lower and thinner, the cloud radiative warming is only about  $10 \text{ Wm}^{-2}$  over land, but  $15 \text{ Wm}^{-2}$  over ocean where there are the stratocumulus regions.

Since in Fig. 14 over ocean the ERBE clear sky LW fluxes are systematically higher than the ones obtained from the ISCCP cloud detection, one would expect a slight overestimation of the cloud radiative warming effect when determined by using the ERBE clear sky identification. However, if one compares Fig. 15 with Fig. 14, the correlation is not straightforward, since an additional uncertainty comes from the different clear sky sampling, especially in regions where clear sky does not appear often. The difference between clear sky flux and total flux can only be determined for regions where there was at least one clear sky occurrence during the month of March. If these regions are not the same within one latitude zone when using different clear sky identifications, such a difference in sampling adds another uncertainty in determining the cloud radiative effects. Around the equator where the ERBE clear sky fluxes are about  $4 \text{ Wm}^{-2}$  higher, the cloud warming can be lower or equal to the one found in combination with original ISCCP data. This can be only explained by the fact that the clear sky scenes found by ERBE are preferentially located in regions where there is less cloudiness. It is interesting to note that the two methods developed for ScaRaB (described in Sections 2c and 2d) lead to very similar clear sky fluxes over ocean (Fig. 14), but show systematic differences of cloud warming of about  $3 \text{ Wm}^{-2}$ . The cloud radiative warming is stronger when clear sky is found by the ScaRaB spatial-resolution-adapted ISCCP cloud detection. This indicates that, by replacing the time statistics with space statistics (within the same geotype) over a smaller time period, clear sky is found more often in regions with smaller cloud amounts. Over land, this effect can be seen in the southern hemisphere, where the last method estimates a  $5 \text{ Wm}^{-2}$  smaller cloud warming than all other methods.

### ***b. Cloud radiative cooling***

Cloud radiative cooling is also examined. Since the SW fluxes depend strongly on the sun elevation and the ScaRaB observation time changes considerably over one month, the SW cooling effect is more difficult to analyze. Clear sky SW albedos (not shown) are between 11 and 17 % over ocean and between 15 and 25 % over land. Similar effects as for the clear sky LW fluxes are produced by the different clear sky detection methods. Over ocean, the ERBE clear sky albedo is systematically the lowest, whereas it is highest in the desert regions and over tropical land. Again, the ScaRaB-adapted clear sky identifications yield scenes with less cloud contamination (lowest clear sky albedo). The radiative cloud cooling in the morning, which is the difference between clear sky SW flux and total SW flux, is presented in Fig. 16. The mean observation time increases slightly from the Northern hemisphere (solar zenith angle  $65^\circ$ ) to the Southern hemisphere (solar zenith angle  $55^\circ$ ). The strongest radiative cooling effect of about  $90 \text{ Wm}^{-2}$  is seen in the tropics over land (also with the strongest warming effect), indicating that the Inter Tropical Convergence Zone (ITCZ) is situated mostly over land in March. Another region of strong cloud cooling can be observed over Southern hemisphere midlatitude oceans, indicating frequent storms and thick low-level clouds. The effect of sampling statistics due to different clear sky identification plays a much smaller role over ocean (differences of about  $5 \text{ Wm}^{-2}$  with exception of Northern hemisphere subtropics where differences range up to  $20 \text{ Wm}^{-2}$ ) than over land. The ERBE-like analysis determines a  $20 \text{ Wm}^{-2}$  stronger cloud cooling over tropical land than all other clear sky identifications. This shows again that clear sky statistics are an important uncertainty factor in determining cloud radiative effects.

### *c. Cloud radiative effects in the tropics*

To finalize our sensitivity study, we show in Fig. 17 tropical (latitude band between 14° N and 14° S) outgoing LW and SW fluxes for clear sky determined by the original ISCCP and ERBE algorithms on ScaRaB data and from original ISCCP data for six months of collocated ScaRaB-ISCCP daytime data. The tropical differences between ERBE clear sky identification and the newly developed ScaRaB methods using the narrow-band channels have been identified in Section 3 as the largest, because the tropics have the highest water vapor abundance. As mentioned in the introduction, the observation time of the Meteor satellite changes during the months: daytime observations were taken around 8 am local time in March, 5 pm in April, 2 pm in May, 11 am in June, 8 am and 6 pm in July and 3 pm in August. Sun zenith viewing angles vary between 60° (in July) and 35° (in May and July). Since the seasonal variation of clear sky temperature in the tropics is small, the variation of the clear sky fluxes as a function of observation month are most probably caused by diurnal variation. From Figures 17a and 17b one concludes that at all these observation times the ERBE clear sky LW fluxes are systematically 4  $\text{Wm}^{-2}$  higher and the SW fluxes 5 to 10  $\text{Wm}^{-2}$  lower than the ones obtained from original ISCCP clear sky. On the other hand, as seen in the sections before, the clear sky identification from the original ISCCP algorithms on the ScaRaB data is slightly cloud contaminated leading to about 1  $\text{Wm}^{-2}$  lower LW fluxes and to 5 to 10  $\text{Wm}^{-2}$  higher SW fluxes than those from original ISCCP clear sky. Assuming the same total fluxes, one would obtain the strongest cloud warming effect and strongest cloud cooling effect using the ERBE clear sky identification. By investigating the tropical cloud radiative effects in Figures 18a and 18b, one observes again that this conclusion is not generally applicable. It is only true in the first three months, whereas the effect is the opposite in the second two months where less cloudy regions have been picked out to represent clear sky

statistics. On a monthly basis the uncertainty due to different clear sky statistics adds another  $4 \text{ Wm}^{-2}$  for the cloud warming and  $5 \text{ Wm}^{-2}$  for the cloud cooling effect.

## 5. Conclusions

Different cloud detection methods making use of the narrow-band channels of the ScaRaB radiometer allow for a sensitivity study on zonally averaged clear sky fluxes at TOA and on cloud radiative effects compared to results using the ERBE clear sky identification. We have seen that the effect on the clear sky LW fluxes is relatively small, but the ERBE method produces a systematically higher clear sky LW flux ( $2$  to  $5 \text{ Wm}^{-2}$ ). Employing the original ISCCP cloud detection on the ScaRaB data shows already that the narrow-band channels are very useful for cloud detection, especially in regions with high water vapor abundance. Adapting the ISCCP method to ScaRaB spatial resolution and to temporal sampling leads to a clear sky identification with less cloud contamination and hence to slightly higher clear sky LW fluxes, but still less than those of ERBE clear sky scenes. However, the determination of cloud radiative effects from flux observations in this manner depends not only on the value of clear sky fluxes but also on clear sky sampling statistics. Whereas clear sky fluxes of all the ScaRaB-adapted clear sky identifications are very close, the cloud radiative warming and cooling can still differ by  $5 \text{ Wm}^{-2}$  and  $10 \text{ Wm}^{-2}$  respectively.

## REFERENCES

- Barkstrom, B. R., E. F. Harrison, G. L. Smith, R. Green, J. Kibler, R. Cess, and the ERBE Science Team, 1989: Earth Radiation Budget Experiment (ERBE) archival and April 1985 results. *Bull. Amer. Meteorol. Soc.*, **70**, 1254-1262.
- Briand, V.: Vers une meilleure exploitation des observations satellitales pour l'étude de l'effet radiatif des nuages, Ph. D. thesis, University of Paris VI, pp. 129. [Available from LMD, Ecole Polytechnique, 91128 Palaiseau, Cedex, France]
- Capderou, M., 1995: Une annee de ScaRaB. Orbitographie et echantillonnage temporel pour le satellite Meteor 3-07/ ScaRaB. LMD Technical Note. [Available from Laboratoire de Meteorologie Dynamique, Ecole Polytechnique, F-91128 Palaiseau cedex, France].
- Chen, T., W. B. Rossow, and Y.-C. Zhang, 2000: Radiative effects of cloud type variations. *J. Climate*, **13**, 264-286.
- Collins, W. D., A. K. Inamdar, 1995: Validation of clear-sky fluxes for tropical oceans from the Earth Radiation Budget Experiment. *J. Climate*, **8**, 569-578.
- Hartmann, D. L., and D. Doelling, 1991: On the net radiative effectiveness of clouds. *J. Geophys. Res.*, **96**, 869-891.
- Harshvardhan, D. A. Randall, T. G. Corsetti, and D. A. Dazlich, 1989: Earth radiation budget and cloudiness simulations with a general circulation model. *J. Atmos. Sci.*, **46**, 1922-1942.
- Kandel, R. and International ScaRaB Scientific Working Group (ISSWG), 1998: The ScaRaB earth radiation budget dataset. *Bull. Amer. Meteor. Soc.*, **79**, 765-783.
- Ockert-Bell, M. E., and D. L. Hartmann, 1992: The effect of cloud type on earth's energy balance: Results for selected regions. *J. Climate*, **5**, 1158-1171.
- Ridout, J. A., B. Chertock, and R. Gelaro, 1994: Response of a general circulation model to a

- change in cloud solar forcing: Model feedbacks and comparison with satellite data, *J. Geophys. Res.*, **99**, 18555-18576.
- Rossow, W. B., L. C. Garder, and A. A. Lacis, 1989: Global, seasonal cloud variations from satellite radiance measurements. Part I: Sensitivity of Analyses. *J. Climate*, **2**, 419-458.
- Rossow, W. B. and R. A. Schiffer, 1991: ISCCP cloud data products. *Bull. Amer. Meteor. Soc.*, **72**, 2-20.
- Rossow, W. B., and L. C. Garder, 1993a: Cloud detection using satellite measurements of infrared and visible radiances for ISCCP. *J. Climate*, **6**, 2341-2369.
- Rossow, W. B., and L. C. Garder, 1993b: Validation of ISCCP cloud detections. *J. Climate*, **6**, 2370-2393.
- Rossow, W. B., A. W. Walker and L. C. Garder, 1993c: Comparison of ISCCP and other cloud amounts. *J. Climate*, **6**, 2394-2418.
- Rossow, W. B. and Y.-C. Zhang, 1995: Calculation of surface and top of atmosphere radiative fluxes from physical quantities based on ISCCP data sets 2. Validation and first results. *J. Geophys. Res.*, **100**, 1167-1197.
- Rossow, W. B. and R. A. Schiffer, 1999: Advances in understanding clouds from ISCCP. *Bull. Amer. Meteor. Soc.*, **80**, 2261-2287.
- Rutan, D. A. and T. P. Charlock, 1997: Spectral reflectance, directional reflectance and broadband albedo of the Earth's surface, *Proceedings of 9th AMS conference on atmospheric radiation*, Long Beach, 446-470.
- Seze, G., and W. B. Rossow, 1991: Effects of satellite data resolution on measuring the space/time variations of surfaces and clouds. *Int. J. Remote Sensing*, **12**, 921-952.
- Smith, G. L., R. N. Green, E. Raschke, L. M. Avis, J. T. Suttles, B. A. Wielicki, and R. Davies, 1986: Inversion method for satellite studies of the earth's radiation budget:

- development of algorithms for the ERBE mission. *J. Geophys. Res.*, **24**, 407-421.
- Stubenrauch, C. J., G. Seze, N. A. Scott, A. Chédin, M. Desbois, and R. S. Kandel, 1996: Cloud field identification for earth radiation budget studies. Part II: cloud field classification for the ScaRaB radiometer. *J. Appl. Meteor.*, **35**, 428-443.
- Stubenrauch, C. J., A. D. Del Genio, and W. B. Rossow, 1997: Implementation of subgrid cloud vertical structure inside a GCM and its effect on the radiation budget. *J. Climate*, **10**, 273-287.
- Stubenrauch, C. J., W. B. Rossow, N. A. Scott, and A. Chédin, 1999: Clouds as seen by infrared sounders (3I) and imagers (ISCCP), III, Spatial heterogeneity and radiative effects. *J. Climate*, **12**, 3419-3442.
- Suttles, J. T. and B. A. Wielicki, 1992: Top-of-atmosphere radiative fluxes : validation of ERBE scanner inversion algorithm using Nimbus-7 ERB data. *J. Appl. Meteor.*, **31**, 784-796.
- Viollier, M., R. S. Kandel, and P. Raberanto, 1995: Inversion and space-time averaging algorithms for ScaRaB (Scanner for Earth Radiation Budget) - Comparison with ERBE, *Ann. Geophys.*, **13**, 959-968.
- Wielicki, B. A. and R. N. Green, 1989: Cloud identification for ERBE radiative flux retrieval. *J. Appl. Meteor.*, **28**, 1133-1146.
- Wielicki, B. A. and L Parker, 1992: On the determination of cloud cover from satellite sensors: the effect of sensor spatial resolution. *J. Geophys. Res.*, **97**, 12799-12823.
- Wielicki, B. A., R. D. Cess, M. D. King, D. A. Randall and E. F. Harrison, 1995: Mission to planet Earth: role of clouds and radiation in climate. *Bull. Amer. Meteor. Soc.*, **76**, 2125-2153.

## Table and Figure Captions

Table 1: Modifications of thresholds in the different steps of the ISCCP cloud detection in order to adapt it for the ScaRaB spatial resolution.

Table 2: Geotypes used to determine clear sky composite radiances in a cloud detection adapted to the ScaRaB temporal sampling and their link to CERES/SARB scene types.

Fig. 1: Illustration of spatial resolution of a ScaRaB pixel and of the sampling of ISCCP pixels (from AVHRR measurements at Global Area Coverage resolution) within a ScaRaB pixel and within a gridbox of  $1^\circ$  latitude  $\times$   $1^\circ$  longitude. The sampling of ISCCP can hide small clouds which escape the measurements.

Fig. 2: Brightness temperature ( $T_B$ ) distributions for original ISCCP data a) of all scenes together and b) only of ISCCP clear sky scenes; and  $T_B$  distributions for ScaRaB data c) of all scenes together and d) only of ISCCP clear sky scenes.

Fig. 3: Distributions of clear sky brightness temperatures subtracted by clear sky composite brightness temperatures a) for original ISCCP data, b) for simulated ScaRaB data (using four adjacent ISCCP pixels), c) for ScaRaB data on which the original ISCCP cloud detection was applied and d) for ScaRaB data using spatial resolution adapted thresholds for the clear sky composite determination.

Fig. 4: Clear sky reference brightness temperature as a function of latitude in March 1994, a) for evergreen forest, b) for grassland, c) for ocean between 90° to 120° longitude and d) for ocean between 210° to 240° longitude.

Fig. 5: Clear sky reference brightness temperature as a function of latitude for the twelve different longitude bands of ocean, in March 1994.

Fig. 6: Clear sky reference brightness temperature as a function of latitude at four time periods, corresponding to different observation times, in March 1994, a) for evergreen forest, b) for grassland c) for ocean between 90° to 120° longitude and d) for ocean between 210° to 240° longitude.

Fig. 7: Scatter plots of a) relative brightness temperature difference compared to the reference and to the local maximum and b) relative reflectance difference compared to the reference and to the local minimum. Light gray squares correspond to clear sky scenes identified by the ScaRaB spatial resolution adapted ISCCP cloud detection. Scene type is evergreen forest.

Fig. 8: Zonally averaged clear sky frequency as determined by the ERBE identification (ScaRaB-ERBE) and by the original ISCCP cloud detection on ScaRaB pixels (ScaRaB-ISCCP) compared to clear sky frequency from original ISCCP data (AVHRR-ISCCP) at close observation time during the second half of March 1994.

Fig. 9: Evolution of clear sky frequency as a function of pixel size. Pixel size is simulated by adjacent ISCCP pixels from AVHRR measurements on NOAA-12. Results are shown for different geographical regions: the latitude band between  $-30^{\circ}$  and  $+30^{\circ}$  for all scenes and for land and ocean separately, the tropics (latitude between  $-10^{\circ}$  and  $+10^{\circ}$ ), northern hemisphere subtropics (latitude between  $10^{\circ}$  and  $30^{\circ}$ ), the convection zone over Indonesia (Warm Pool) and stratocumulus regions (ST).

Fig. 10: Zonally averaged clear sky frequency as obtained from ERBE identification (ScaRaB-ERBE), original ISCCP (ScaRaB-ISCCP), spatial resolution adapted ISCCP identification (ScaRaB-ISCCP/spat.) and temporal resolution adapted method (ScaRaB-temp.) over ScaRaB pixels, separately over land and ocean, for day measurements in March 1994. Clear sky differences between the first three methods and the ScaRaB-temp. method are also shown.

Fig. 11: Zonally averaged clear sky LW fluxes at TOA as obtained from ERBE identification (ScaRaB-ERBE), original ISCCP (ScaRaB-ISCCP), spatial resolution adapted ISCCP identification (ScaRaB-ISCCP/spat.) and temporal resolution adapted method (ScaRaB-temp.) over ScaRaB pixels, separately over land and ocean, for day measurements in March 1994. Clear sky flux differences between the first three methods and the ScaRaB-temp. method are also shown.

Fig. 12: Zonally averaged clear sky LW fluxes at TOA as obtained from ERBE identification (ScaRaB-ERBE), original ISCCP (ScaRaB-ISCCP), spatial resolution adapted ISCCP identification (ScaRaB-ISCCP/spat.) and temporal resolution adapted method

(ScaRaB-temp.) over ScaRaB pixels, separately over land and ocean, for night measurements in March 1994. Clear sky flux differences between the first three methods and the ScaRaB-temp. method are also shown.

Fig. 13: Clear sky frequency as a function of latitude a) for ocean and b) for land. Clear sky over a ScaRaB pixel is identified by ERBE (ScaRaB-ERBE), original ISCCP (ScaRaB-ISCCP), ISCCP modified to spatial resolution (ScaRaB-ISCCP/spat.), algorithm for temporal resolution (ScaRaB-temp.), compared to fluxes for collocated ISCCP clear sky scenes (ISCCP). The clear sky frequency corresponds to the fraction of  $4^\circ \times 5^\circ$  regions which have clear sky extending over at least a  $1^\circ \times 1^\circ$  region. Clear sky differences between the four methods applied to ScaRaB and original ISCCP are also shown.

Fig. 14: Clear sky outgoing LW fluxes at TOA as a function of latitude a) for ocean and b) for land. Clear sky over a ScaRaB pixel is identified by ERBE (ScaRaB-ERBE), original ISCCP (ScaRaB-ISCCP), ISCCP modified to spatial resolution (ScaRaB-ISCCP/spat.), algorithm for temporal resolution (ScaRaB-temp.), compared to fluxes for collocated ISCCP clear sky scenes (ISCCP).  $1^\circ$  clear sky fluxes are first averaged over regions of  $4^\circ \times 5^\circ$ . Clear sky flux differences between the four methods applied to ScaRaB and original ISCCP are also shown.

Fig. 15: Cloud radiative warming as a function of latitude a) for ocean and b) for land. Clear sky over a ScaRaB pixel is identified by ERBE (ScaRaB-ERBE), original ISCCP (ScaRaB-ISCCP), ISCCP modified to spatial resolution (ScaRaB-ISCCP/spat.), algorithm for temporal resolution (ScaRaB-temp.), compared to fluxes for collocated ISCCP clear sky

scenes (ISCCP). Statistics from regions of  $4^\circ \times 5^\circ$  are considered. Cloud radiative warming differences obtained from the four clear sky methods applied to ScaRaB and original ISCCP are also shown.

Fig. 16: Cloud radiative cooling as a function of latitude a) for ocean and b) for land. Clear sky over a ScaRaB pixel is identified by ERBE (ScaRaB-ERBE), original ISCCP (ScaRaB-ISCCP), ISCCP modified to spatial resolution (ScaRaB-ISCCP/spat.), algorithm for temporal resolution (ScaRaB-temp.), compared to fluxes for collocated ISCCP clear sky scenes (ISCCP). Statistics from regions of  $4^\circ \times 5^\circ$  are considered. Cloud radiative cooling differences obtained from the four clear sky methods applied to ScaRaB and original ISCCP are also shown.

Fig. 17: Outgoing clear sky fluxes in the tropics (latitude band from  $14^\circ$  N to  $14^\circ$  S) as a function of observation month a) LW and b) SW. Clear sky over a ScaRaB pixel is identified by ERBE (ScaRaB-ERBE), original ISCCP (ScaRaB-ISCCP), compared to fluxes for collocated ISCCP clear sky scenes (ISCCP). Statistics from regions of  $4^\circ \times 5^\circ$  are considered.

Fig. 18: a) Cloud radiative warming and b) cloud radiative cooling in the tropics (latitude band from  $14^\circ$  N to  $14^\circ$  S) as a function of observation month. Clear sky over a ScaRaB pixel is identified by ERBE (ScaRaB-ERBE), original ISCCP (ScaRaB-ISCCP), compared to fluxes for collocated ISCCP clear sky scenes (ISCCP). Statistics from regions of  $4^\circ \times 5^\circ$  are considered.

**Table 1**

Algorithm part	Parameter	Original value		Value for ScaRaB	
		land	ocean	land	ocean
Temporal variability test	$\Delta 2$	2.0	1.0	0.8	0.4
	$\Delta 3$	8.0	3.5	3.0	1.0
IR composite logic	short term - $\Delta 2$	5.0	2.0	3.3	1.3
	long term - $\Delta 3$	8.0	2.5	5.3	2.7
VIS composite logic	short term - $\Delta 1$	6.0	3.0	4.0	2.0
	long term - $\Delta 2$	3.5	1.5	2.3	1.0
Final thresholds	IR	4.0	2.5	1.5	1.0
	VIS	6.0	3.0	4.0	2.0

Table 1: Modifications of thresholds in the different steps of the ISCCP cloud detection in order to adapt it for the ScaRaB spatial resolution.

**Table 2**

geotype	CERES/SARB geotype
evergreen forest	1, 2
deciduous forest	3 - 5
bushland	6, 7
savanna	8, 9
grasslands	10 - 14
tundra	18
desert	16
partial snow / ice	ISCCP partial snow
total snow / ice	15 and ISCCP total snow
ocean	17

Table 2: Geotypes used to determine clear sky composite radiances in a cloud detection adapted to the ScaRaB temporal sampling and their link to CERES/SARB scene types.

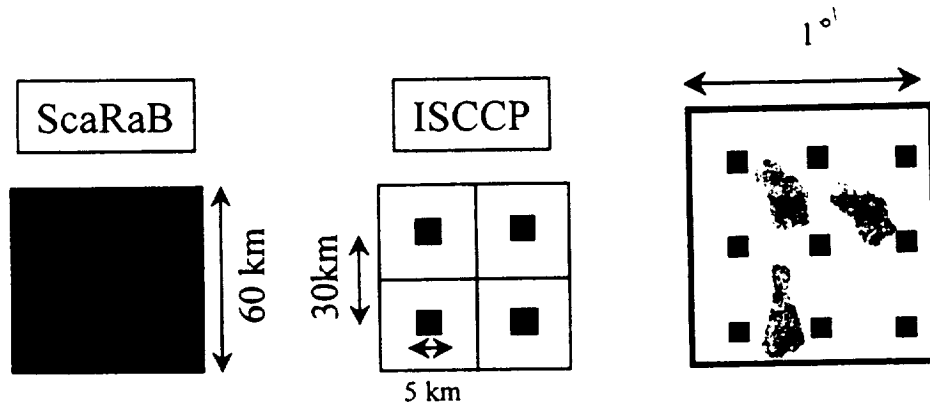


Fig. 1: Illustration of spatial resolution of a ScaRaB pixel and of the sampling of ISCCP pixels (from AVHRR measurements at Global Area Coverage resolution) within a ScaRaBpixel and within a gridbox of  $1^\circ$  latitude  $\times$   $1^\circ$  longitude. The sampling of ISCCP can hide small clouds which escape the measurements.

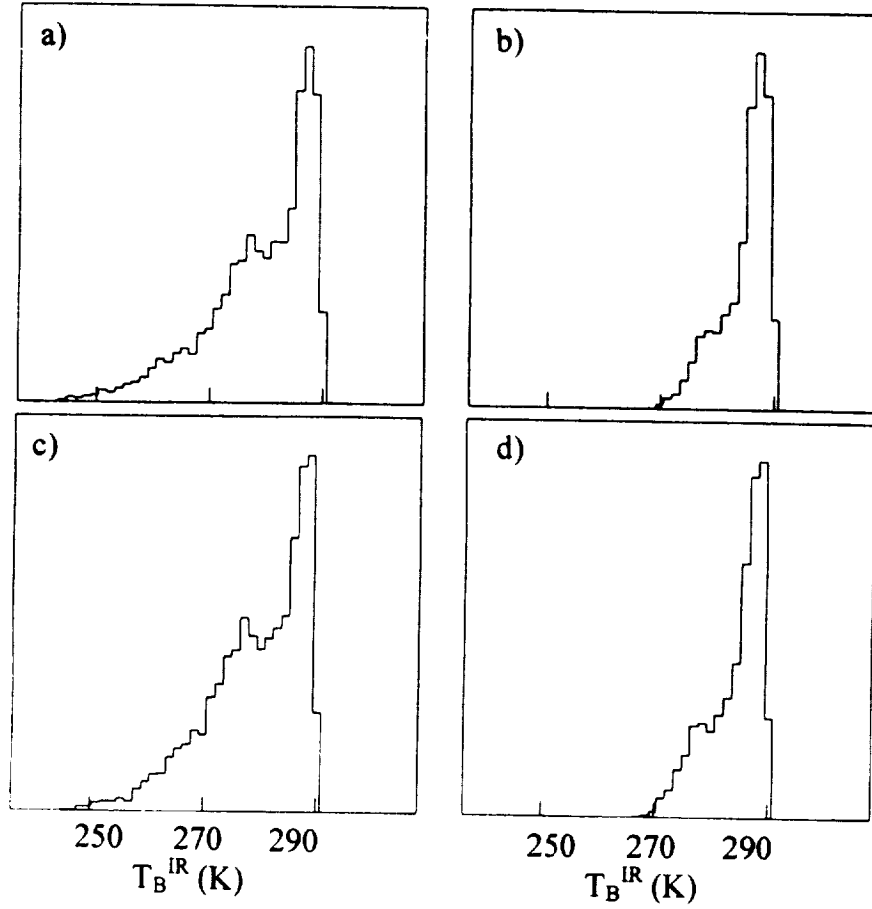


Fig. 2: Brightness temperature ( $T_B$ ) distributions for original ISCCP data a) of all scenes together and b) only of ISCCP clear sky scenes; and  $T_B$  distributions for ScaRaB data c) of all scenes together and d) only of ISCCP clear sky scenes.

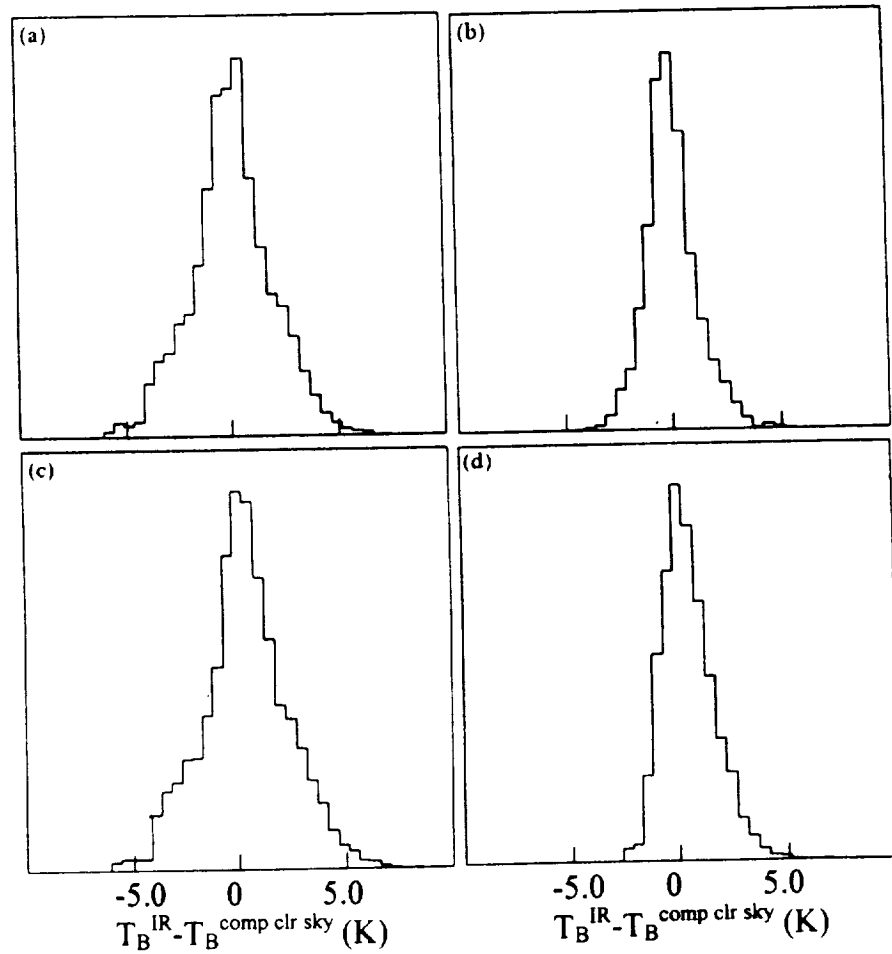


Fig. 3: Distributions of clear sky brightness temperatures subtracted by clear sky composite brightness temperatures a) for original ISCCP data, b) for simulated ScaRaB data (using four adjacent ISCCP pixels), c) for ScaRaB data on which the original ISCCP cloud detection was applied and d) for ScaRaB data using spatial resolution adapted thresholds for the clear sky composite determination.

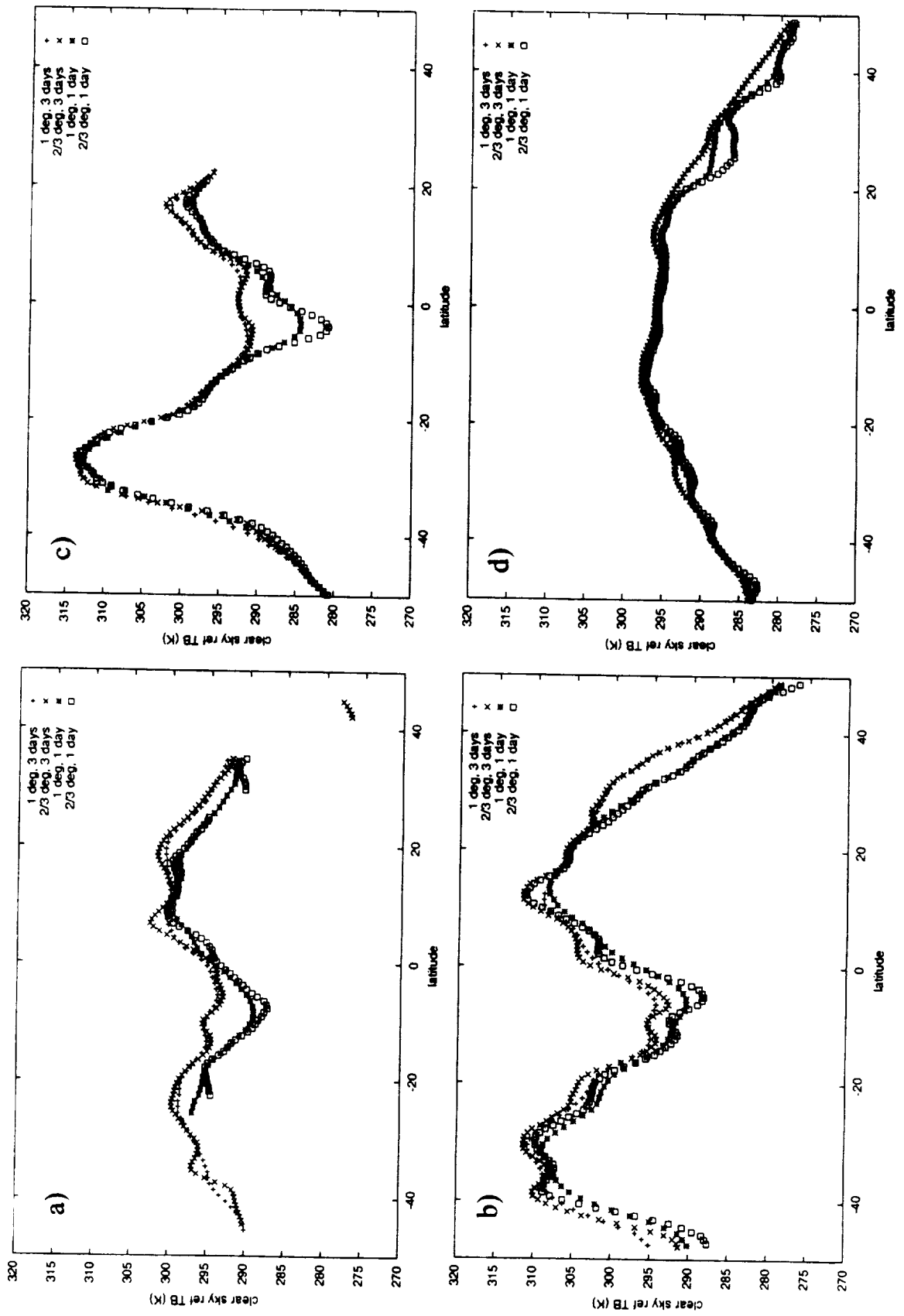


Fig. 4: Clear sky reference brightness temperature as a function of latitude in March 1994, a) for evergreen forest, b) for grassland, c) for ocean between 90° to 120° longitude and d) for ocean between 210° to 240° longitude.

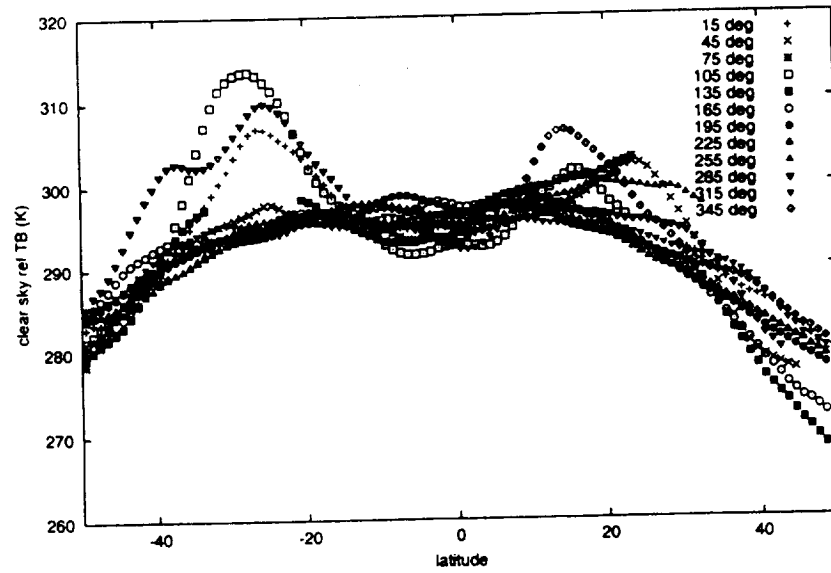


Fig. 5: Clear sky reference brightness temperature as a function of latitude for the twelve different longitude bands of ocean, in March 1994.

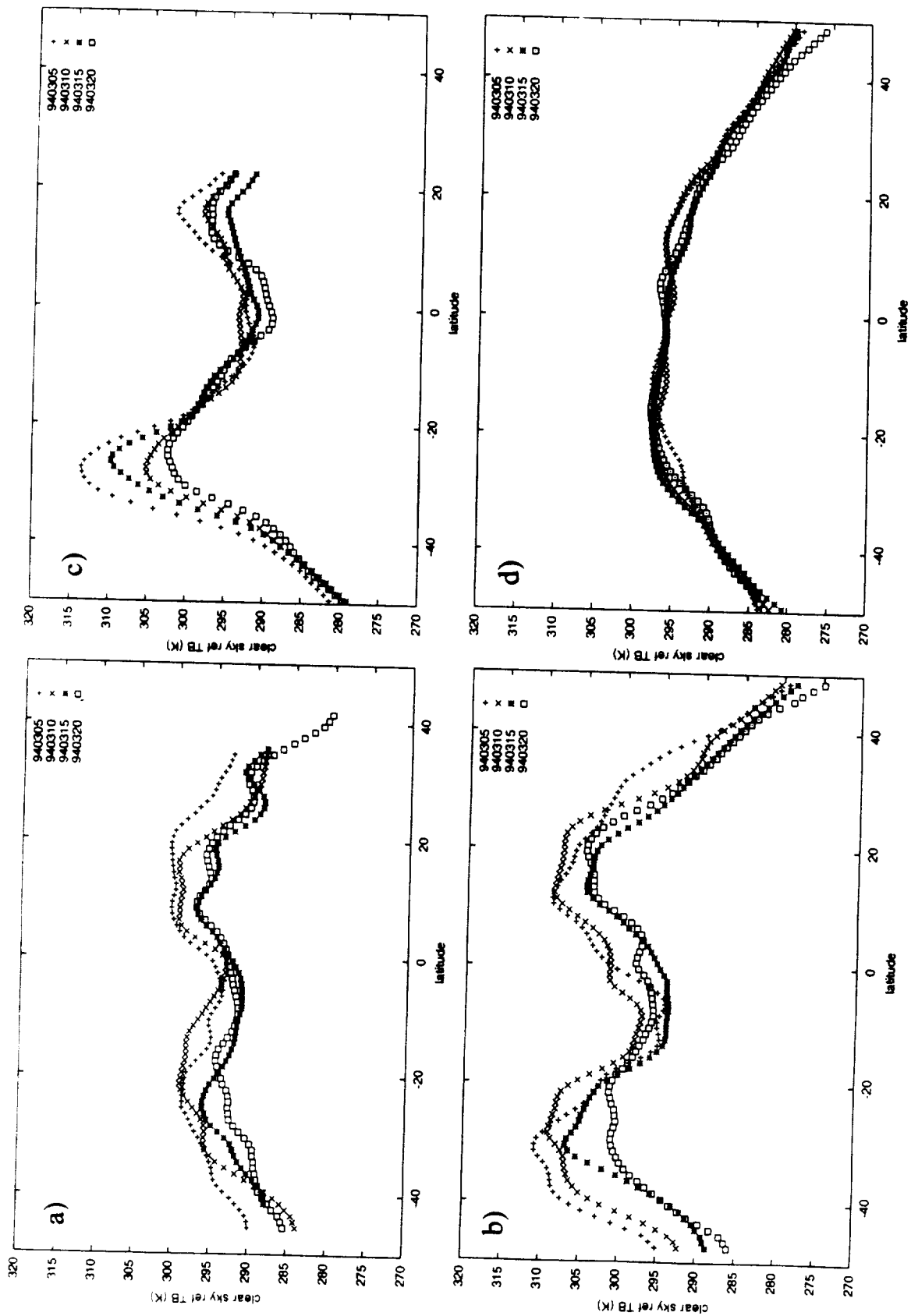


Fig. 6: Clear sky reference brightness temperature as a function of latitude at four time periods, corresponding to different observation times, in March 1994, a) for evergreen forest, b) for grassland c) for ocean between 90° to 120° longitude and d) for ocean between 210° to 240° longitude.

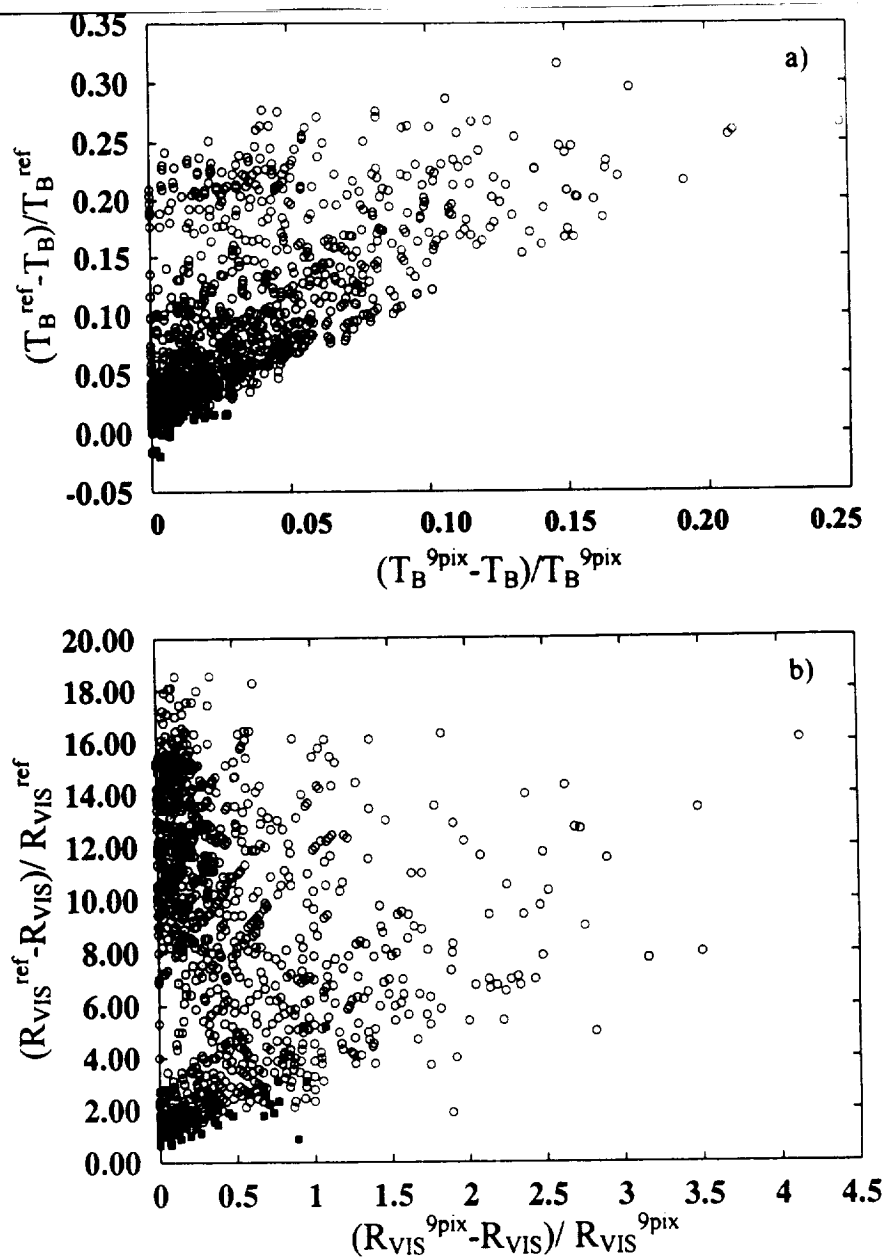


Fig. 7: Scatter plots of a) relative brightness temperature difference compared to the reference and to the local maximum and b) relative reflectance difference compared to the reference and to the local minimum. Light gray squares correspond to clear sky scenes identified by the ScaRaB spatial resolution adapted ISCCP cloud detection. Scene type is evergreen forest.

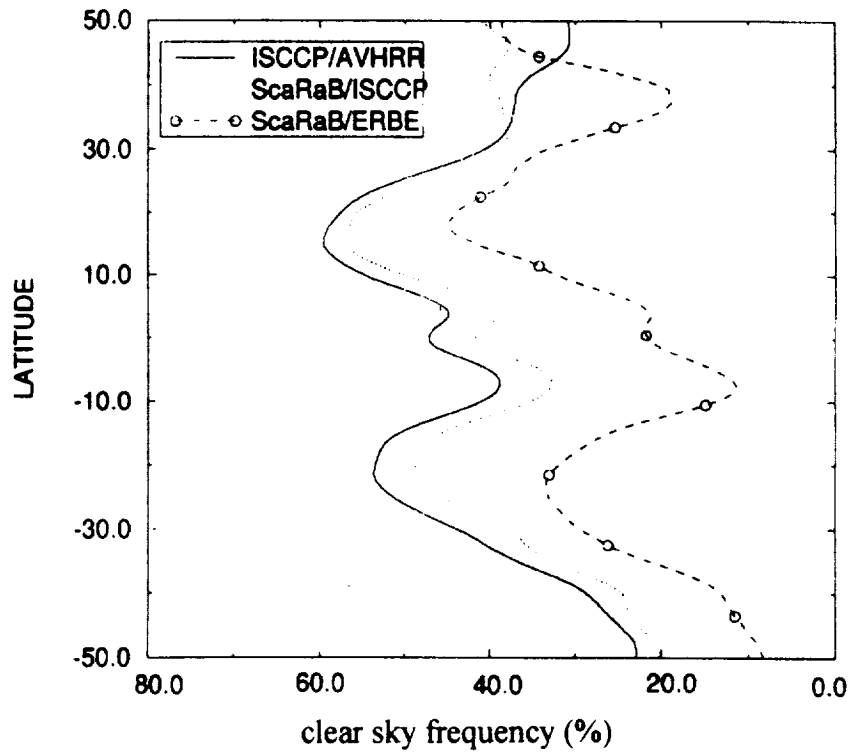


Fig. 8: Zonally averaged clear sky frequency as determined by the ERBE identification (ScaRaB-ERBE) and by the original ISCCP cloud detection on ScaRaB pixels (ScaRaB-ISCCP) compared to clear sky frequency from original ISCCP data (AVHRR-ISCCP) at close observation time during the second half of March 1994.

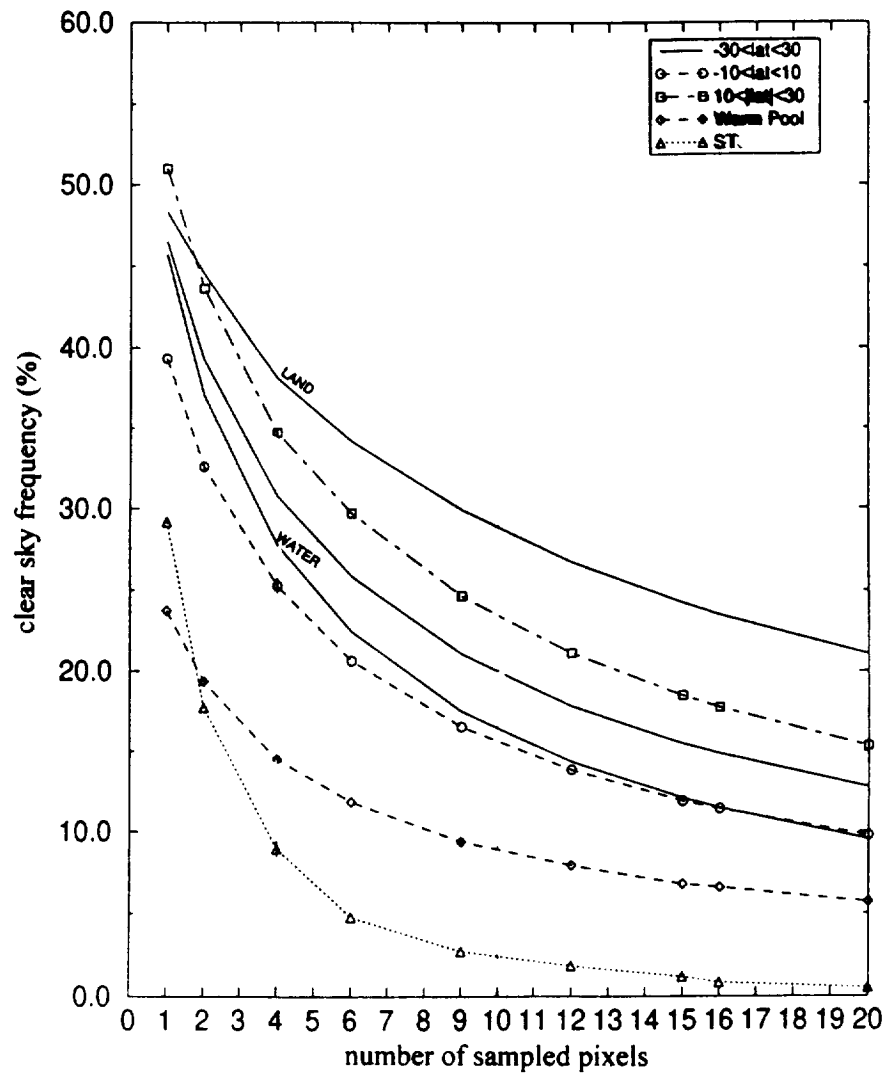


Fig. 9: Evolution of clear sky frequency as a function of pixel size. Pixel size is simulated by adjacent ISCCP pixels from AVHRR measurements on NOAA-12. Results are shown for different geographical regions: the latitude band between  $-30^\circ$  and  $+30^\circ$  for all scenes and for land and ocean separately, the tropics (latitude between  $-10^\circ$  and  $+10^\circ$ ), northern hemisphere subtropics (latitude between  $10^\circ$  and  $30^\circ$ ), the convection zone over Indonesia (Warm Pool) and stratocumulus regions (ST).

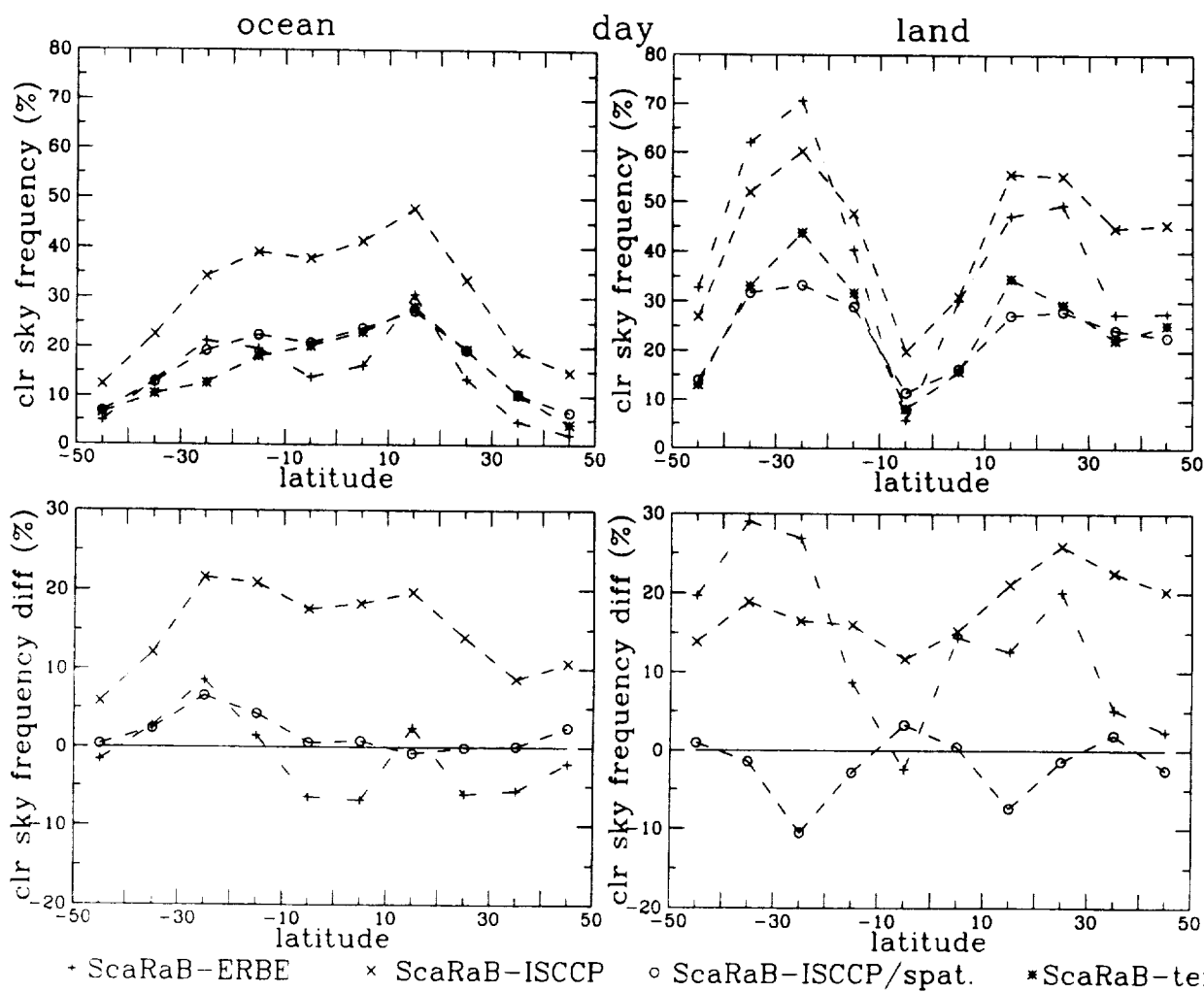


Fig. 10: Zonally averaged clear sky frequency as obtained from ERBE identification (ScaRaB-ERBE), original ISCCP (ScaRaB-ISCCP), spatial resolution adapted ISCCP identification (ScaRaB-ISCCP/spat.) and temporal resolution adapted method (ScaRaB-temp.) over ScaRaB pixels, separately over land and ocean, for day measurements in March 1994. Clear sky differences between the first three methods and the ScaRaB-temp. method are also shown.

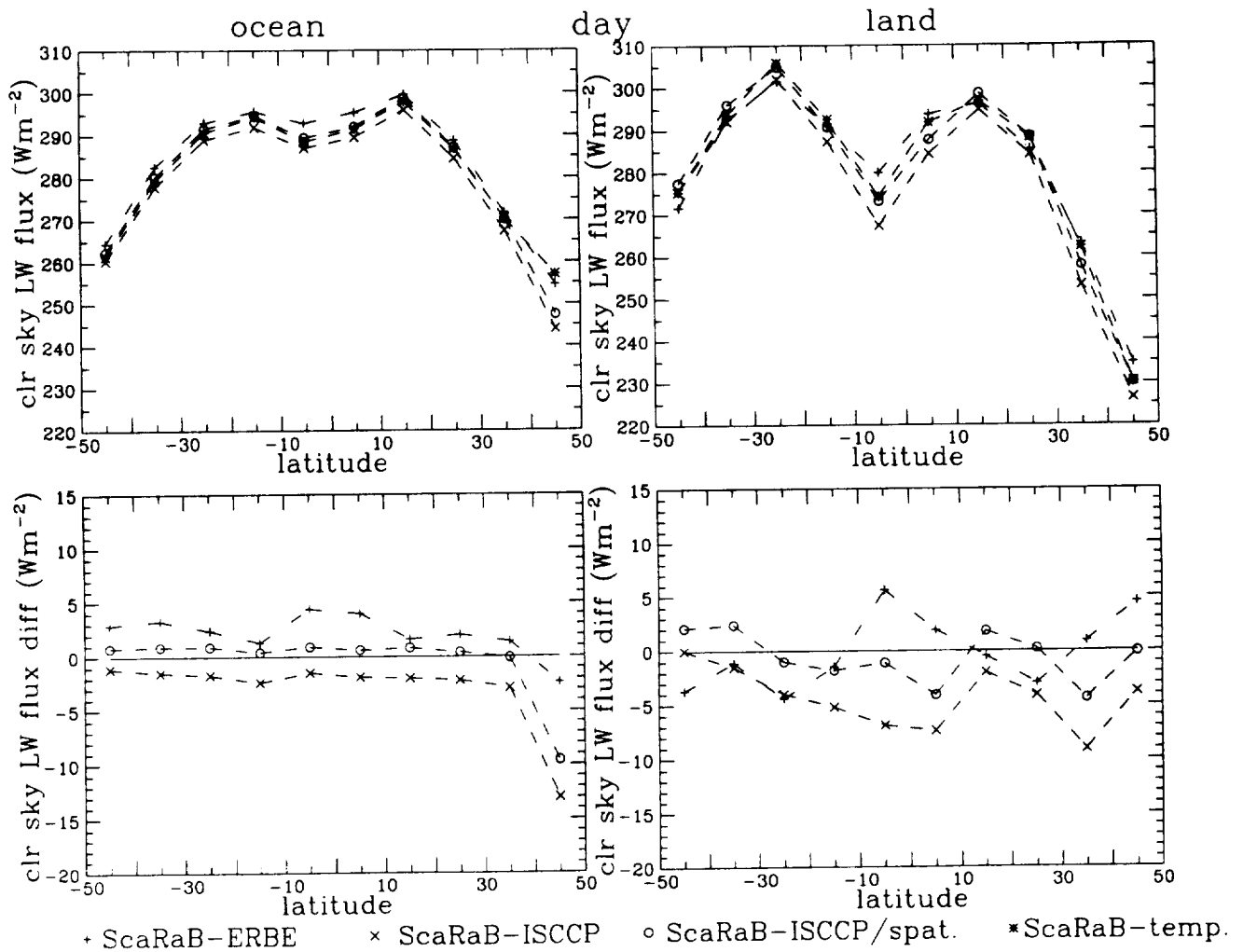


Fig. 11: Zonally averaged clear sky LW fluxes at TOA as obtained from ERBE identification (ScaRaB-ERBE), original ISCCP (ScaRaB-ISCCP), spatial resolution adapted ISCCP identification (ScaRaB-ISCCP/spat.) and temporal resolution adapted method (ScaRaB-temp.) over ScaRaB pixels, separately over land and ocean, for day measurements in March 1994. Clear sky flux differences between the first three methods and the ScaRaB-temp. method are also shown.

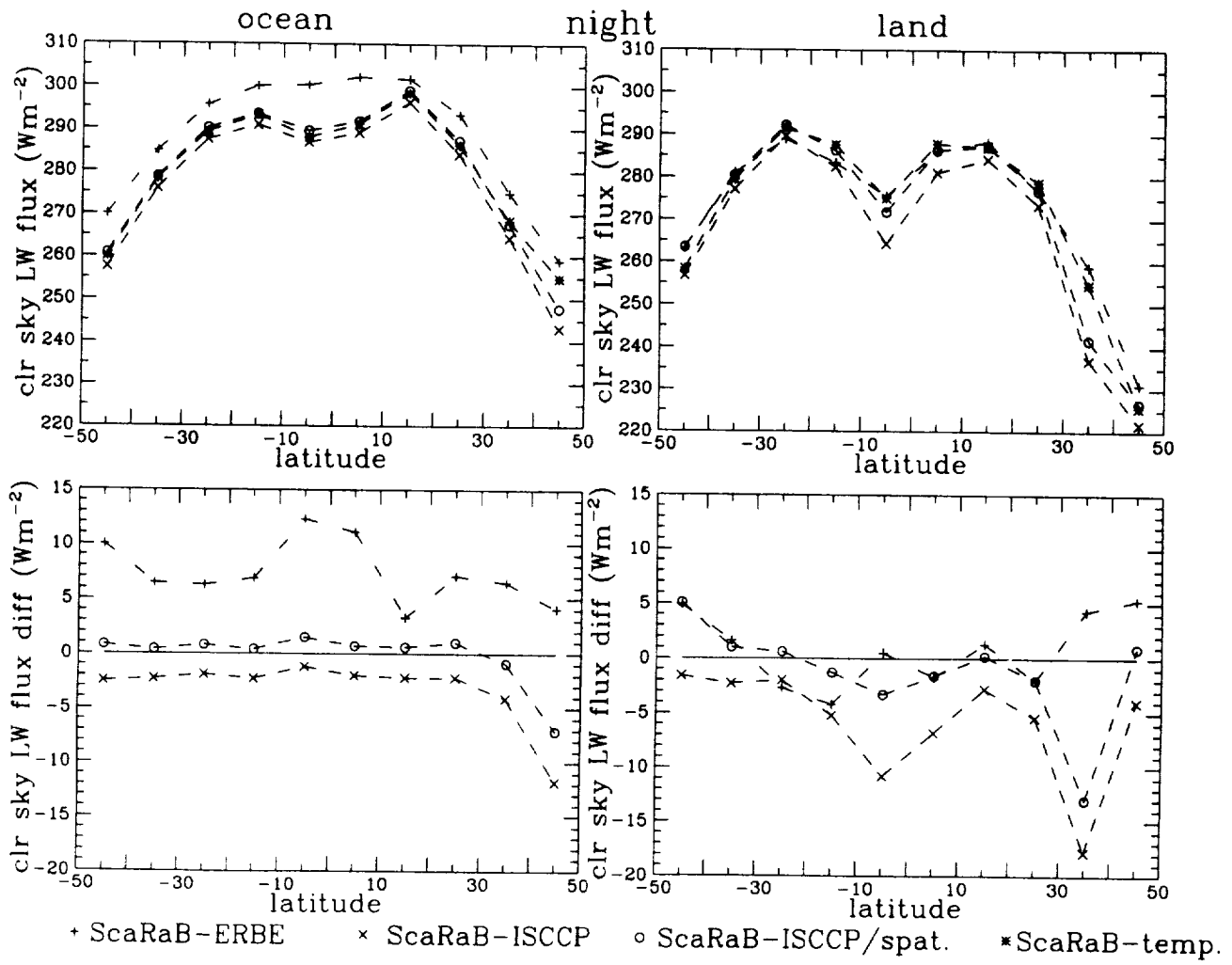


Fig. 12: Zonally averaged clear sky LW fluxes at TOA as obtained from ERBE identification (ScaRaB-ERBE), original ISCCP (ScaRaB-ISCCP), spatial resolution adapted ISCCP identification (ScaRaB-ISCCP/spat.) and temporal resolution adapted method (ScaRaB-temp.) over ScaRaB pixels, separately over land and ocean, for night measurements in March 1994. Clear sky flux differences between the first three methods and the ScaRaB-temp. method are also shown.

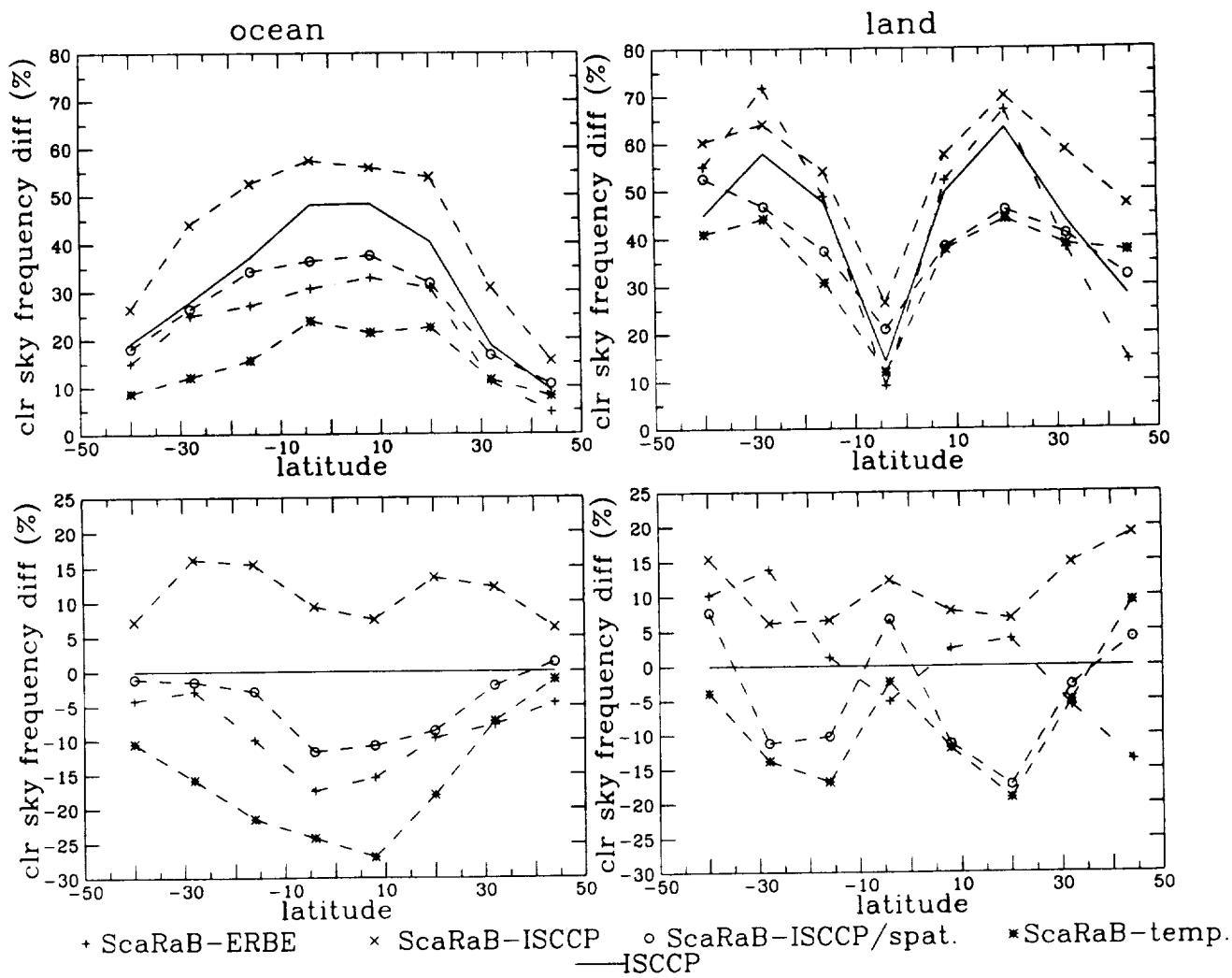


Fig. 13: Clear sky frequency as a function of latitude a) for ocean and b) for land. Clear sky over a ScaRaB pixel is identified by ERBE (ScaRaB-ERBE), original ISCCP (ScaRaB-ISCCP), ISCCP modified to spatial resolution (ScaRaB-ISCCP/spat.), algorithm for temporal resolution (ScaRaB-temp.), compared to fluxes for collocated ISCCP clear sky scenes (ISCCP). The clear sky frequency corresponds to the fraction of  $4^\circ \times 5^\circ$  regions which have clear sky extending over at least a  $1^\circ \times 1^\circ$  region. Clear sky differences between the four methods applied to ScaRaB and original ISCCP are also shown.

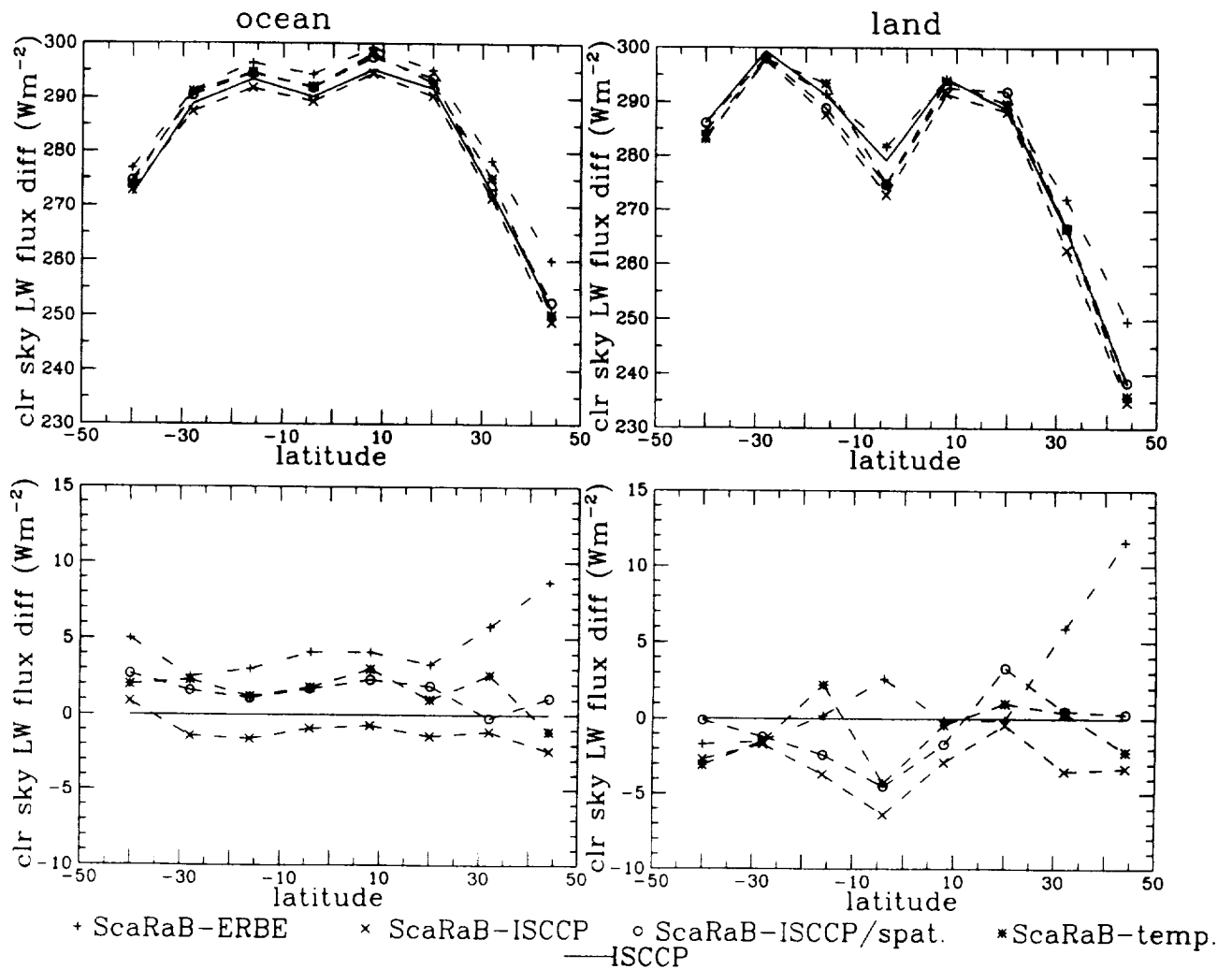


Fig. 14: Clear sky outgoing LW fluxes at TOA as a function of latitude a) for ocean and b) for land. Clear sky over a ScaRaB pixel is identified by ERBE (ScaRaB-ERBE), original ISCCP (ScaRaB-ISCCP), ISCCP modified to spatial resolution (ScaRaB-ISCCP/spat.), algorithm for temporal resolution (ScaRaB-temp.), compared to fluxes for collocated ISCCP clear sky scenes (ISCCP). 1° clear sky fluxes are first averaged over regions of 4° x 5°. Clear sky flux differences between the four methods applied to ScaRaB and original ISCCP are also shown.

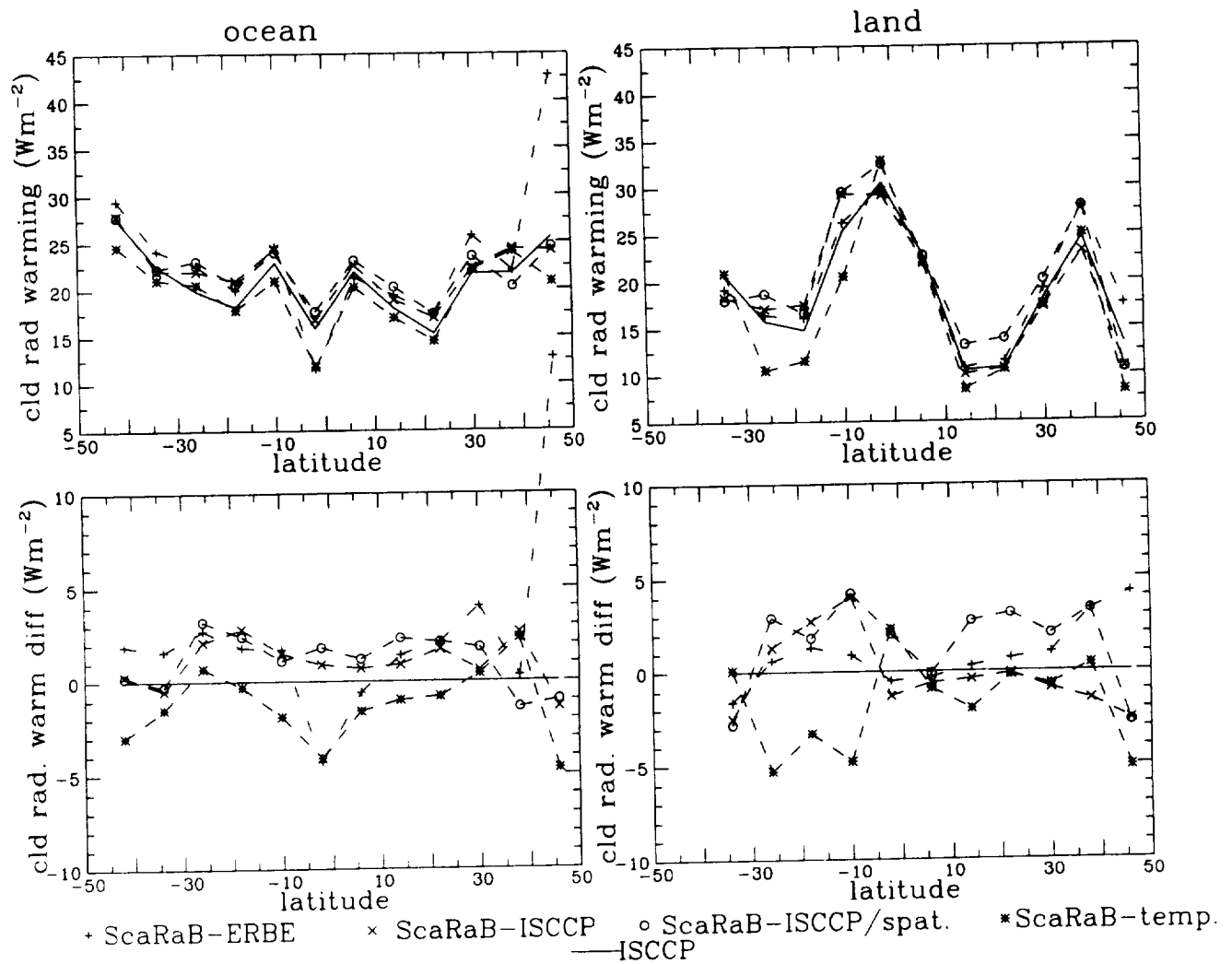


Fig. 15: Cloud radiative warming as a function of latitude a) for ocean and b) for land. Clear sky over a ScaRaB pixel is identified by ERBE (ScaRaB-ERBE), original ISCCP (ScaRaB-ISCCP), ISCCP modified to spatial resolution (ScaRaB-ISCCP/spat.), algorithm for temporal resolution (ScaRaB-temp.), compared to fluxes for collocated ISCCP clear sky scenes (ISCCP). Statistics from regions of  $4^{\circ} \times 5^{\circ}$  are considered. Cloud radiative warming differences obtained from the four clear sky methods applied to ScaRaB and original ISCCP are also shown.

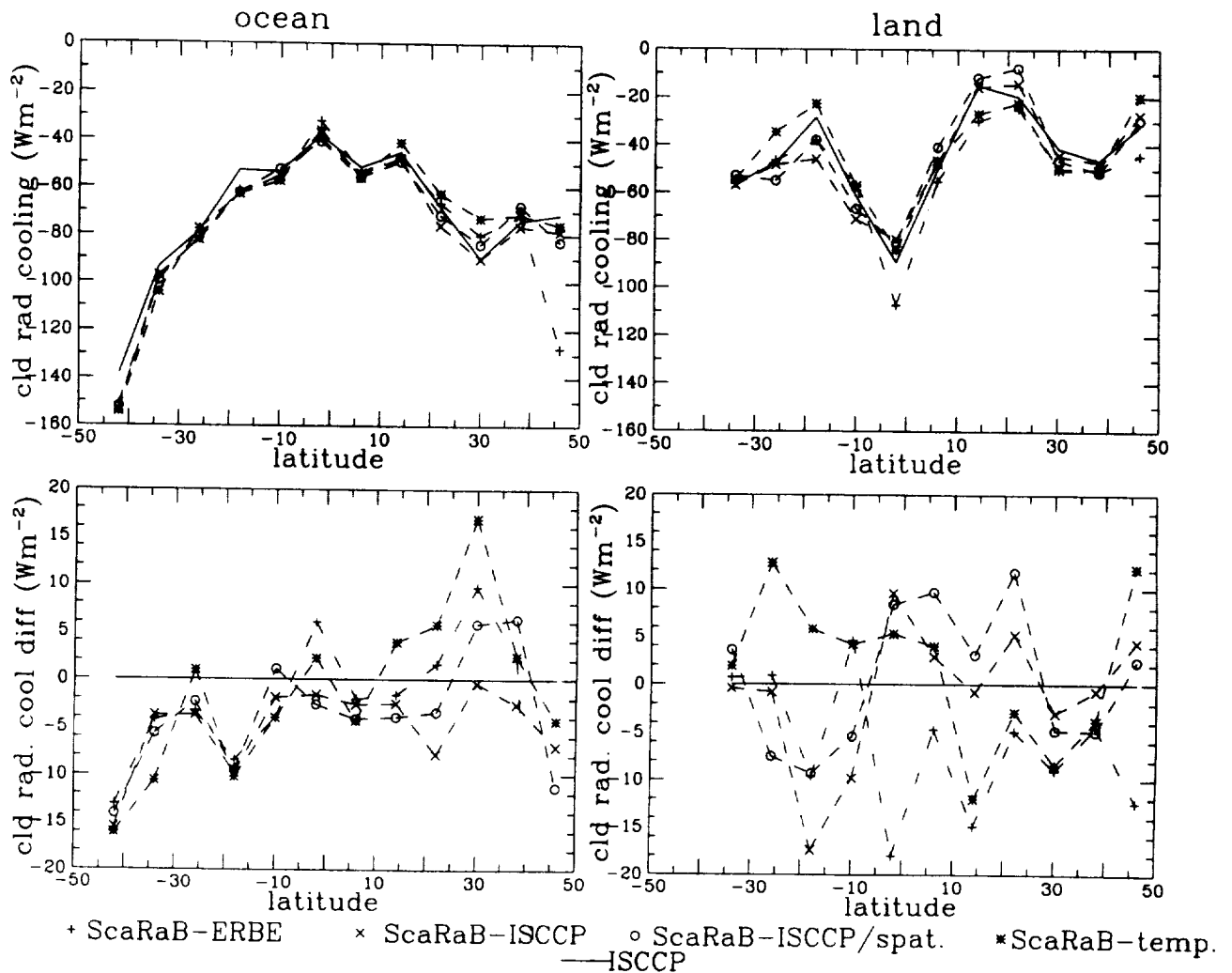


Fig. 16: Cloud radiative cooling as a function of latitude a) for ocean and b) for land. Clear sky over a ScaRaB pixel is identified by ERBE (ScaRaB-ERBE), original ISCCP (ScaRaB-ISCCP), ISCCP modified to spatial resolution (ScaRaB-ISCCP/spat.), algorithm for temporal resolution (ScaRaB-temp.), compared to fluxes for collocated ISCCP clear sky scenes (ISCCP). Statistics from regions of  $4^{\circ} \times 5^{\circ}$  are considered. Cloud radiative cooling differences obtained from the four clear sky methods applied to ScaRaB and original ISCCP are also shown.

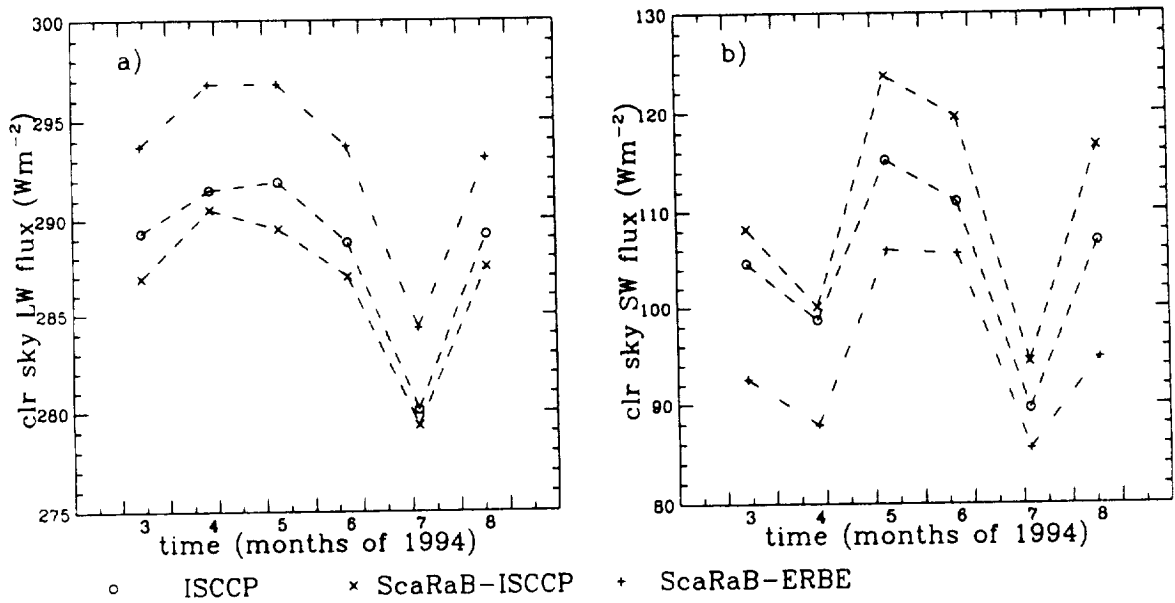


Fig. 17: Outgoing clear sky fluxes in the tropics (latitude band from 14° N to 14° S) as a function of observation month a) LW and b) SW. Clear sky over a ScaRaB pixel is identified by ERBE (ScaRaB-ERBE), original ISCCP (ScaRaB-ISCCP), compared to fluxes for collocated ISCCP clear sky scenes (ISCCP). Statistics from regions of 4° x 5° are considered.

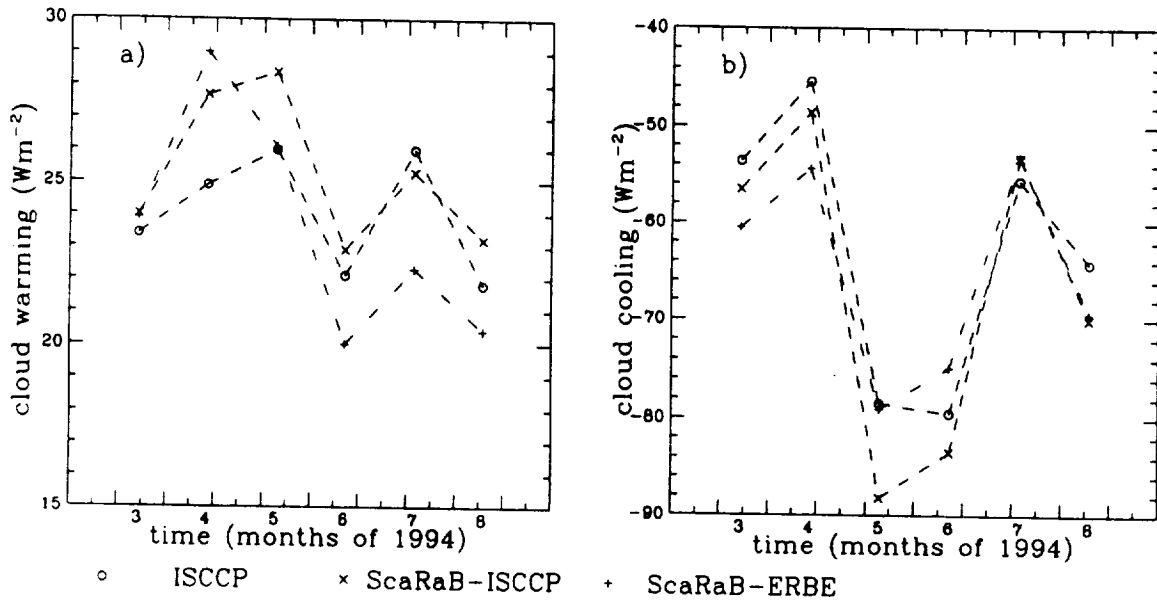


Fig. 18: a) Cloud radiative warming and b) cloud radiative cooling in the tropics (latitude band from 14° N to 14° S) as a function of observation month. Clear sky over a ScaRaB pixel is identified by ERBE (ScaRaB-ERBE), original ISCCP (ScaRaB-ISCCP), compared to fluxes for collocated ISCCP clear sky scenes (ISCCP). Statistics from regions of 4° x 5° are considered.